Reorganisation of turbulence by large and spanwise-varying riblets

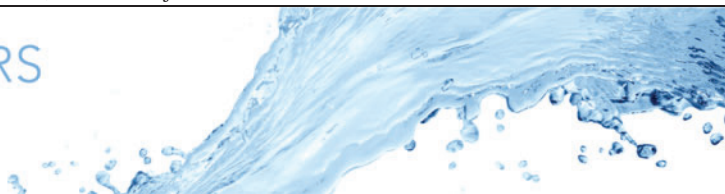Endrikat, S.; Newton, R. ; Modesti, D.; García-Mayoral, R.; Hutchins, N.; Chung, D.

Important note
To cite this publication, please use the final published version (if applicable).
Please check the document version above.

JM PAPERS

Reorganisation of turbulence by large and spanwise-varying riblets

S. Endrikat[1], **R. Newton**[1], **D. Modesti**[1,2], **R. García-Mayoral**[3], **N. Hutchins**[1] **and D. Chung**[1,†]

[1]Department of Mechanical Engineering, University of Melbourne, Victoria 3010, Australia

[2]Faculty of Aerospace Engineering, Delft University of Technology, 2629 HS, Delft, Netherlands

[3]Department of Engineering, University of Cambridge, Cambridge CB2 1PZ, UK

We study the flow above non-optimal riblets, specifically large drag-increasing and two-scale trapezoidal riblets. In order to reach large Reynolds numbers and large scale separation while retaining access to flow details, we employ a combination of boundary-layer hot-wire measurements and direct numerical simulation (DNS) in minimal-span channels. Although the outer Reynolds numbers differ, we observe fair agreement between experiments and DNS at matched viscous–friction-scaled riblet spacings s^+ in the overlapping physical and spectral regions, providing confidence that both data sets are valid. We find that hot-wire velocity spectra above very large riblets with $s^+ \gtrsim 60$ are depleted of near-wall energy at scales that are (much) greater than s. Large-scale energy likely bypasses the turbulence cascade and is transferred directly to secondary flows of size s, which we observe to grow in strength with increasing riblet size. Furthermore, the present very large riblets reduce the von Kármán constant κ of the spanwise uniform mean velocity in a logarithmic layer and, thus, reduce the accuracy of the roughness-function concept, which we link to the near-wall damping of large flow structures. Half-height riblets in the groove, which we use as a model of imperfectly repeated (spanwise-varying) riblets, impede in-groove turbulence. We show how to scale the drag optimum of imperfectly repeated riblets based on representative measurements of the true geometry by solving inexpensive Poisson equations.

Key words: drag reduction, turbulent boundary layers

† Email address for correspondence: daniel.chung@unimelb.edu.au

1. Introduction

Riblets are streamwise-aligned grooves on a surface that modify wall-bounded turbulent flow. Depending on their viscous–friction-scaled size, riblets can reduce or increase drag compared with a smooth wall. Viscous–friction scaling, denoted in this study by a '+' superscript, employs the kinematic viscosity ν and mean friction velocity $u_\tau \equiv \sqrt{\tau_w/\rho}$ with constant fluid density ρ and mean wall-shear stress (drag per unit plan area) τ_w. The flow over riblets has been investigated extensively in laboratory experiments (e.g. Walsh & Weinstein 1978; Suzuki & Kasagi 1994; Bechert *et al.* 1997; Lee & Lee 2001), numerical simulations (e.g. Choi, Moin & Kim 1993; Chu & Karniadakis 1993; Goldstein & Tuan 1998; García-Mayoral & Jiménez 2011*b*; Endrikat *et al.* 2021*b*) and model calculations (e.g. Luchini, Manzo & Pozzi 1991; Tullis & Pollard 1993; Chavarin & Luhar 2019; Ran, Zare & Jovanović 2021).

1.1. *Large drag-increasing and imperfectly repeated riblets*

So far, most studies primarily focused on the drag-reducing regime of small and perfectly repeated riblets, that is, in near-optimal conditions. Off-design conditions are less studied. Large riblets constitute a limiting case of wall roughness and imperfectly repeated riblets challenge the physical ideas behind models that estimate the drag change or an equivalent boundary condition. We analyse these two off-design conditions: large drag-increasing and imperfectly repeated riblets.

One recent study on drag-increasing riblets that are very large in viscous–friction scaling is by Gatti *et al.* (2020), who acquired channel flow pressure-drop measurements in air for trapezoidal riblets with spacings $8 \lesssim s^+ \lesssim 111$. They observe that riblets appear to exhibit a fully rough behaviour for only a finite range of sizes, beyond which the drag curve peels off from the expected fully rough asymptote. Local hot-wire measurements inside the riblet groove, which revealed how very large riblets interact with the flow, were first reported by Newton, Chung & Hutchins (2018).

Two-scale (also called 'brother-and-sister') riblets were initially devised for improved maximum drag reduction, but the oil-channel experiments by Bruse *et al.* (1993) showed that they have roughly the same minimum skin friction as single-scale riblets. We revisit two-scale riblets starting at sizes around the drag optimum as an idealisation of imperfectly repeated riblets towards estimating the drag performance due to manufacturing inaccuracies such as varying riblet heights. Possible manufacturing techniques are limited by difficulties in fabricating a large area of accurately repeated riblets with minimal variation (West, Sammut & Tang 2018), but accepting a lower quality makes manufacturing faster and more economical (Kaakkunen *et al.* 2018). Tiainen *et al.* (2020) measured shape variation statistics of imperfect riblets manufactured with nanosecond laser ablation on a curved airfoil. Their riblet heights are in the range 0.71–1.28 times the nominal height and they verified in laboratory experiments that the surface nevertheless reduces drag. Without costly drag measurements, however, *a priori* model estimates of the expected drag or optimal riblet size for given flow conditions assume ideally repeated riblets with a well-defined cross-sectional area, for which the drag reduction relative to a smooth wall follows a near-universal curve (as shown by García-Mayoral & Jiménez 2011*a*). A more accurate drag estimate based on geometry statistics would provide confidence that riblets manufactured with a given technique could reduce drag in full-scale applications without the need for high-fidelity data.

1.2. *Outer-layer similarity and the roughness function*

Most roughness as well as drag-reducing riblets only modify turbulence in a region close to the surface termed the roughness sublayer. One common measure of the roughness-sublayer height is the inhomogeneity of the mean flow (e.g. Raupach, Thom & Edwards 1980; Pokrajac *et al.* 2006; Chan *et al.* 2018; Sharma & García-Mayoral 2020). Any measure of the roughness-sublayer height depends on the flow quantity, but it generally scales with the element spacing rather than the element height (Raupach *et al.* 1980; Raupach, Antonia & Rajagopalan 1991), as further supported by direct numerical simulations (DNS) of spanwise-aligned bars (MacDonald *et al.* 2018) and post arrays (Sharma & García-Mayoral 2020). For riblets, Modesti *et al.* (2021) find that the roughness sublayer of mean secondary (spanwise inhomogeneous) flows extends to a height of about 0.5*s* above the virtual origin of turbulence or, equivalently, the zero-plane displacement (Raupach *et al.* 1991; Jiménez 2004; Chung *et al.* 2021), which is consistent with the study of sinusoidal roughness by Chan *et al.* (2018). Higher-order statistics may be affected up to greater heights.

The outer layer of the flow above the roughness sublayer, however, is similar to that above a smooth wall and the logarithmic layer, which is common to the inner and the outer layer, has a slope that is characterised by the same von Kármán constant $\kappa \approx 0.40$ for both rough and smooth walls. This similarity is a consequence of Townsend's (1956) hypothesis applied to the flow over relatively small roughness (for which the boundary-layer thickness δ far exceeds the roughness or riblet height k and the friction Reynolds number is high). Contrarily, the hot-wire velocity profiles by Newton *et al.* (2018) suggest that very large riblets modify the mean velocity also in the outer layer, although their conclusions are burdened by uncertainties about the friction velocity. Without outer-layer similarity, the roughness function $U^+_{smooth} - U^+$ does not have a constant value ΔU^+ throughout the logarithmic layer. A constant ΔU^+ permits full-scale predictions from scaled experiments or simulations (Flack & Schultz 2014; Chung *et al.* 2021) by encapsulating the drag difference between two surfaces (Hama 1954; Clauser 1956), which is supposedly independent of the outer Reynolds number (Spalart & McLean 2011; García-Mayoral, Gómez-de-Segura & Fairhall 2019).

A lack of outer-layer similarity, either in the mean or fluctuations, has been reported over non-transitionally rough porous surfaces (Manes, Poggi & Ridolfi 2011), large-pitch transverse bars (Krogstadt & Antonia 1999; Krogstad & Efros 2012; Flack & Schultz 2014) and wavy roughness (Napoli, Armenio & De Marchis 2008; Schultz & Flack 2009; Nugroho *et al.* 2021), among others. In some of these cases (Krogstad & Efros 2012; Nugroho *et al.* 2021), outer-layer similarity has been recovered with an even larger scale separation than the oft-quoted $\delta/k \gg 40$ (Jiménez 2004). One way to understand the stricter criterion for recovery is the presence of a much larger length scale than k, such as pitch or wavelength of waviness, which sets the size of the roughness sublayer that is correspondingly much larger than the oft-quoted $2k$–$3k$ (Chung *et al.* 2021). Notably, for the riblets of Newton *et al.* (2018), the largest length scale of the surface is $s = 2k$ and the mean-flow inhomogeneity is confined to $0.5s = 0.5(2k) = k \lesssim \delta/47$ (based on Modesti *et al.* 2021).

1.3. *Outline*

In the present study we extend the analysis of Newton *et al.* (2018) and mitigate uncertainties related to the friction velocity by employing a drag balance together with hot-wire measurements (§ 2.1) and combining this with DNS at a comparatively low friction Reynolds number, but with accurately measured friction velocities (§ 2.2).

In § 3.1 we observe a depletion of large-scale energy in hot-wire spectra even at heights above riblet-induced mean-flow inhomogeneity (§ 3.2). Combining hot-wire and DNS data sets gives us confidence that the present large s^+ riblets modify the statistically spanwise uniform mean flow in the logarithmic layer (§ 3.3) despite the large scale separation $\delta \gg k$ and a high friction Reynolds number. We propose an explanation in § 3.4. The investigation of turbulence also inside of large riblet grooves leads to a model for the average crest (slip) velocity in § 3.5, that can be used to crudely estimate ΔU^+. In § 4 two-scale riblets allow us to also investigate effects of spanwise variations of riblet surfaces on the drag curve. We propose a method for estimating the optimal size of imperfectly manufactured riblets with negligible computational cost, that builds on the hydraulic length ℓ_H from García-Mayoral & Jiménez (2011*b*)

Throughout this paper, x, y and z refer to the streamwise, spanwise and wall-normal directions with corresponding velocity components u, v and w.

2. Experimental and numerical set-ups

2.1. *Hot-wire anemometry in boundary layers*

Experiments were performed in an open-return boundary-layer wind tunnel in the Walter Bassett Aerodynamics lab at the University of Melbourne. The test section has dimensions $5.7\,\text{m} \times 0.94\,\text{m} \times 0.38\,\text{m}$ (streamwise $\times$ spanwise $\times$ wall normal) with measurements made in the boundary layer developed over the lower surface. Full details of this facility are available in Harun *et al.* (2013). The test surface comprises of two $1.89\,\text{m} \times 0.94\,\text{m}$ (streamwise $\times$ spanwise) and three $0.63\,\text{m} \times 0.94\,\text{m}$ tiles of acetal copolymer into which the trapezoidal riblet geometry with $s/k = 2$, tip angle $\alpha = 30°$ and $s = 2.73\,\text{mm}$ (figure 1*a*) is machined using a custom made trapezoidal end mill. The boundary layer is tripped with a strip of P36 grit sandpaper at the inlet to the working section where the riblet surface starts and all measurements are made 4 m downstream of this trip. For the present cases, the flow adjusts to the riblet surface over a streamwise distance of about 50–60 times the boundary-layer thickness before reaching the measurement location. Nominally zero pressure gradient conditions are established by adjusting the flexible perspex ceiling of the working section. Static pressure taps located every $\Delta x = 0.5\,\text{m}$ (between streamwise distance $x = 0\,\text{m}$ and $x = 5.5\,\text{m}$) along the ceiling are used to measure the local pressure difference $\Delta p = p_0 - p$, where p_0 is the local static pressure at $x = 0$ (the entrance to the working section), from which the pressure coefficient C_p is computed ($\equiv 2\Delta p/\rho U_\infty^2$, where U_∞ is the free-stream velocity and ρ is the air density). For all measurements reported here (riblet surfaces with $U_\infty \in [5, 25]\,\text{m s}^{-1}$ in table 1), $C_p = 0 \pm 0.06$.

Boundary-layer profiles are acquired using hot-wire anemometry above both the crest and trough of the riblet geometry (figure 1). Each profile consists of measurements at 50 logarithmically spaced wall-normal locations z. For the measurements over the trough, the wall-normal starting position for the traverse is below the roughness crest. A modified Dantec 55P05 probe has Wollaston wire with $2.5\,\mu\text{m}$ diameter platinum core soldered across the probe tips. The $0.5\,\text{mm}$ ($\approx 0.18s$) active sensor length is exposed by etching the silver jacket using nitric acid solution, yielding a length-to-diameter ratio of 200 (as recommended by Ligrani & Bradshaw 1987). Since the same probe was used at all free-stream velocities, the viscous-scaled sensor length l^+ increases with U_∞ (see table 1). Possible spanwise positioning errors over the crest and trough, and also uncertainty in the etched sensor length l, are explored in the Appendix. The hot-wire probe is operated in constant temperature mode with an overheat ratio of 1.8 using an in-house designed
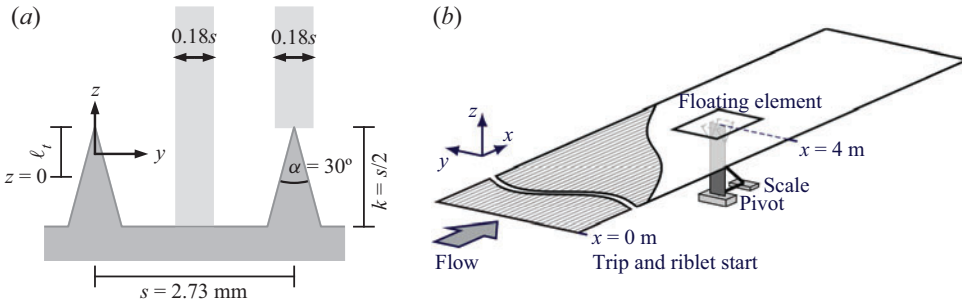
Figure 1. (*a*) Cross-sectional sketch of the riblet surface in the wind tunnel. The shaded areas indicate the spanwise extent and two locations of the active sensor of the hot-wire probe as it traverses in the wall-normal direction. (*b*) Sketch of the test section with the riblet surface and drag balance consisting of a floating element, an arm with its pivot and a digital scale.

Case	U_∞ (m s^{-1})	ν (m^2 s^{-1})	u_τ (m s^{-1})	δ'_{99} (m)	δ'^+_{99}	s^+	δ'_{99}/k	l^+
5	5.0	1.59×10^{-5}	0.21	0.065	850	36	47.6	7
7	7.5	1.60×10^{-5}	0.31	0.065	1250	53	47.4	10
10	10.0	1.61×10^{-5}	0.40	0.066	1640	68	48.6	12
15	15.0	1.59×10^{-5}	0.60	0.064	2420	103	47.0	19
20	19.8	1.60×10^{-5}	0.78	0.062	3000	132	45.3	24
25	24.6	1.59×10^{-5}	0.96	0.063	3840	165	46.4	30

Table 1. Wind tunnel and flow parameters for the hot-wire measurements. For all cases, the spacing-to-height ratio of the riblets is $s/k = 2$ and the tip angle $\alpha = 30°$. The mean friction velocity u_τ is measured using a drag balance. The 99 % boundary-layer thickness δ'_{99} is measured from the virtual origin, here assumed to be $\ell_t = k/2$ below the riblet crest. The etched (active) length of the hot wire is $l = 0.5$ mm.

Melbourne University constant temperature anemometer (MUCTA). The fluctuating voltage signal output from the MUCTA is sampled at a frequency $f = 50$ kHz yielding a viscous-scaled sample interval $0.05 \lesssim \Delta t^+ \lesssim 1.16$ for the range of $5 < U_\infty < 25$ m s^{-1}, where $\Delta t^+ = u_\tau^2/(f\nu)$, to ensure adequate resolution of the highest frequencies. Adequate convergence of low frequency turbulent energy (following Hutchins *et al.* 2009) is achieved with a sampling duration T of 150s, which corresponds to $11\,000 \lesssim TU_\infty/\delta'_{99} \lesssim 58\,000$ for the present range of free-stream velocities. The hot-wire sensor is calibrated *in situ* prior to and after each boundary layer traverse by positioning the hot wire in the free stream of the flow adjacent to a Pitot-static tube. Calibration coefficients are obtained by fitting a third-order polynomial to the mean voltage from the MUCTA and Pitot-static tube measured velocity. During the boundary layer traverse experiment, temperature-based interpolation is applied between pre- and post-calibration curves to compensate for any temperature drift. The time average of the acquired streamwise velocity at two y positions is denoted by $U(y, z)$. When comparing to a smooth-wall flow, the (virtual) origin of z is required, which we denote to be ℓ_t below the riblet tips (figure 1*a*). We generally consider all locations between the groove bottom and riblet crest, but arbitrarily assume $\ell_t = k/2$ to show profiles for only one realistic origin in some figures, as done by, for example, Squire *et al.* (2016*b*) for hot-wire measurements above sandpaper roughness. The assumption is employed for figures 3, 4, 8, 9 and 11, but does affect any conclusions drawn based on them.

The mean friction velocity u_τ is measured using a custom designed cantilever type drag balance of a similar design to that described in Krogstad & Efros (2010). This device has a long moment arm (0.4 m) to maximise sensitivity to the wall-shear stress and minimise sensitivity to any normal forces due to local pressure gradients in the facility. Wall-shear stress was measured on a floating element of size 0.43 m × 0.29 m with either a smooth or riblet surface. The gap width surrounding this floating element was <1 mm throughout, and the use of a restorative balance ensured that this gap does not change with U_∞. The upstream and downstream edges of the floating element tile are chamfered (undercut) to minimise moments due to pressure forces at the gaps. The drag balance is validated for the smooth surface, with the balance-measured results exhibiting agreement with u_τ obtained from Clauser fitted profiles to within ±2 % when $U_\infty \approx 5\ \mathrm{m\,s^{-1}}$, improving to ±0.2 % when $U_\infty \approx 25\ \mathrm{m\,s^{-1}}$.

2.2. *Direct numerical simulations of minimal-channel flow*

We conduct DNS of turbulent and fully developed open channel flow to obtain the flow field over riblets with varying spacing s^+ at friction Reynolds numbers of $\delta^+ \equiv \delta u_\tau/\nu = 395$ and $\delta^+ = 1000$ (table 2). Here, $\delta = z_\delta - z_m$ is the cross-sectional area per channel width, i.e. the half-channel height measured from the riblet mean height z_m (figure 2). Our data set comprises single-scale trapezoidal riblets with a tip angle $\alpha = 30°$ (case names TAs^+) and two-scale trapezoidal riblets (TMs^+) that have one additional half-sized riblet with the same tip angle in the centre of the groove. We previously analysed parts of this data set in (Endrikat *et al.* 2021*a*; Modesti *et al.* 2021). The numerical domain is sketched in figure 2 and geometrical parameters including domain extents are given in table 2. Simulations of smooth-wall flow at matching friction Reynolds numbers serve as a common reference.

The Navier–Stokes equations for an incompressible fluid

$$\frac{\partial \boldsymbol{u}}{\partial t} + \boldsymbol{\nabla} \cdot (\boldsymbol{uu}) = -\frac{1}{\rho}\boldsymbol{\nabla}p + \nu\nabla^2\boldsymbol{u} - \frac{1}{\rho}\frac{\mathrm{d}P}{\mathrm{d}x}\boldsymbol{e_x}, \quad \boldsymbol{\nabla}\cdot\boldsymbol{u} = 0, \tag{2.1a,b}$$

are solved using the finite volume code Cliff by Cascade Technologies Inc. (Ham, Mattsson & Iaccarino 2006; Ham *et al.* 2007). The velocity $\boldsymbol{u}$ has components (u, v, w) in the streamwise (x), spanwise (y) and wall-normal (z) direction and time is t. A constant pressure gradient $\mathrm{d}P/\mathrm{d}x$ drives the flow in the streamwise direction indicated by $\boldsymbol{e_x}$ and p is the fluctuating component of pressure that we solve for.

The overline $\overline{(\cdot)}(z)$ denotes averages in t, x and y at one height z above the riblet crest. In analogy to the hot-wire data, $U(y, z)$ is the mean velocity averaged in t, x and over the spanwise extent of the hot-wire probe, $0.18s$, either centred around $y = s/2$ (centred above troughs) or around $y = s$ (centred above riblet tips). Inside the roughness sublayer, $\bar{u}(z) \neq U(z)$ because $\overline{(\cdot)}$ averages over s and the hot-wire averages only over $0.18s$. Above the roughness sublayer, the flow is statistically spanwise uniform and the averages over the two regions are equal. Furthermore, $\widetilde{u}\widetilde{w} = \langle u \rangle \langle w \rangle - \bar{u}\bar{w}$ denotes the dispersive component of Reynolds stress, which cannot be measured by a single hot wire, because it is due to the xt-averaged spatial variation $\langle \cdot \rangle (y, z)$ about $\overline{(\cdot)}(z)$ and here $\bar{w} = 0$ so $\widetilde{u}\widetilde{w} = \langle u \rangle \langle w \rangle$.

All simulations are conducted in minimal-span channels (Jiménez & Moin 1991; Flores & Jiménez 2010; Hwang 2013), which reduces the computational cost of evaluating the flow over roughness compared with using full-span channels (MacDonald *et al.* 2017). The flow above $z_c^+ = 0.4L_y^+$, where L_y is the spanwise domain extent, is unphysically constricted in narrow domains (Chung *et al.* 2015), but the flow field close to the wall is

Cross-section	Case	s^+	k^+	k_1^+	ℓ_g^+	$\ell_{g,i}^+$	Δx^+	Δy^+	Δz^+	$\Delta t^+ (\times 10^3)$	L_x^+	L_y^+	δ^+	δ'^+	ℓ_t^+	$L_t u_t/\delta$	$\Delta U^+ \pm \zeta^+$	$\varepsilon'^+ (\times 10^3)$
△△	TA18	17.9	8.93	0.0	11.8	11.8	6.0	0.27–3.0	0.31–7.0	47.4	2054	250	395.0	390.5	4.47	50.1	−0.99 ± 0.10	4.2
△△	TA31	31.3	15.6	0.0	20.6	20.6	6.0	0.47–2.4	0.31–7.0	47.4	2054	250	395.0	387.2	7.81	46.7	+0.56 ± 0.10	3.4
△△	TA36	36.5	18.2	0.0	24.0	24.0	6.0	0.55–2.9	0.31–7.1	47.4	2054	255	395.0	385.9	9.12	49.2	+0.96 ± 0.10	4.5
△△	TA50	50.0	25.0	0.0	32.9	32.9	6.0	0.76–3.9	0.31–7.1	47.4	2054	250	395.0	382.5	12.50	45.7	+1.98 ± 0.10	5.9
△△	TA63	62.5	31.3	0.0	41.1	41.1	6.0	0.95–4.9	0.31–7.1	47.4	2054	250	395.0	379.4	15.63	46.7	+2.75 ± 0.10	7.3
△△	TA100	100	50.0	0.0	65.8	65.8	6.0	0.58–4.0	0.31–8.7	47.5	2000	600	1000.0	975.0	25.00	19.2	+3.66 ± 0.10	8.4
△△	TA150	150	75.0	0.0	98.7	98.7	6.0	0.52–3.8	0.32–8.8	47.5	2000	600	1000.0	962.5	37.50	23.0	+4.18 ± 0.09	11
△△△	TM12	12.5	6.25	3.12	8.07	6.98	6.0	0.089–1.6	0.31–7.0	19.8	2054	250	395.0	391.9	3.12	37.4	−0.77 ± 0.11	4.8
△△△	TM17	16.7	8.33	4.17	10.8	9.31	6.0	0.064–2.1	0.31–7.0	13.8	2054	250	395.0	390.8	4.17	37.3	−0.88 ± 0.11	4.5
△△△	TM21	20.8	10.4	5.21	13.4	11.6	6.0	0.086–2.6	0.31–7.1	15.8	2054	250	395.0	389.8	5.21	37.3	−0.89 ± 0.11	3.5
△△△	TM25	25.0	12.5	6.25	16.1	14.0	6.0	0.11–3.1	0.31–7.1	15.8	2054	250	395.0	388.8	6.25	37.5	−0.57 ± 0.11	3.0
△△△	TM31	31.2	15.6	7.81	20.2	17.5	6.0	0.14–1.9	0.31–7.1	23.7	2054	250	395.0	387.2	7.81	37.4	−0.01 ± 0.11	3.3
△△△	TM36	36.5	18.2	9.12	23.5	20.4	6.0	0.18–2.2	0.31–7.1	27.6	2054	255	395.0	385.9	9.12	39.2	+0.42 ± 0.11	4.8
△△△	TM42	41.7	20.8	10.4	26.9	23.3	6.0	0.21–2.4	0.31–7.1	27.6	2054	250	395.0	384.6	10.42	45.2	+0.72 ± 0.10	3.4
△△△	TM62	62.5	31.2	15.6	40.3	34.9	6.0	0.39–2.8	0.31–7.0	47.4	2054	250	395.0	379.4	15.62	37.6	+2.12 ± 0.11	3.7
	S395	—	—	—	—	—	6.0	3.0	0.21–4.7	79.0	1027	250	395.0	—	—	173	—	3.6
	S1000	—	—	—	—	—	6.0	3.0	0.32–8.8	80.0	2000	600	1000.0	—	—	58.5	—	3.3

Table 2. Simulation parameters for the single-scale (TA) and multi-scale (TM) riblet configurations and smooth wall (S) reference flow. Riblet spacing s^+, heights k^+ and k_1^+ and sizes ℓ_g^+ (square root of the groove cross-sectional area) and $\ell_{g,i}^+$ (figure 12 for $k_1/k = \{0, 0.5\}$). Mesh spacings Δ and domain extents L. The half-channel height $\delta^+ = L_z^+$ is measured from the riblet mean height and δ'^+ from the virtual origin (here assumed $\ell_t = k/2$ below the riblet tips). The total averaging time following initial discarded transients L_t determines the statistical uncertainty ζ^+ of ΔU^+ (MacDonald *et al.* 2017). The drag change ΔU^+ is measured at the critical height $z_c^+ = 0.4L_y^+$ of these minimal-span channels. Statistical convergence is measured by ε'^+, the average error of the streamwise mean momentum balance (Vinuesa *et al.* 2016) above the highest riblet crest.
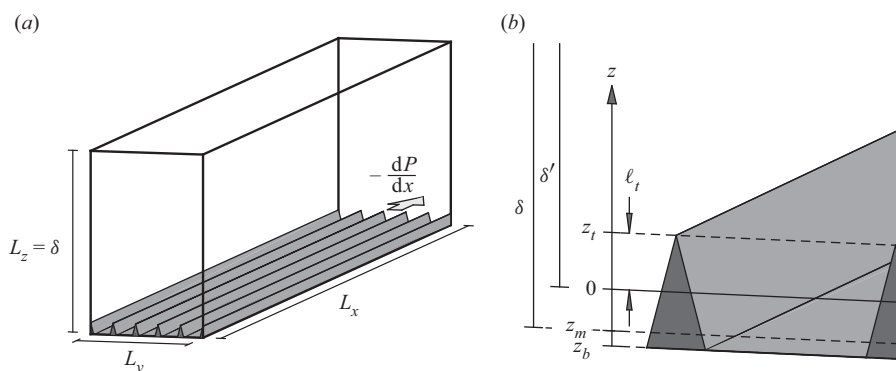
Figure 2. (*a*) Spanwise-minimal numerical domain of case TA50, which has five riblets with $s^+ = 50$ across the span. (*b*) Sketch illustrating the wall-normal coordinate with the bottom of the groove $z = z_b$, the mean height $z = z_m$, the virtual origin $z = 0$ and the riblet tips $z = z_t$. The half-channel height δ is measured from the mean height and δ' from the virtual origin, ℓ_t below the tips.

representative of that in full-span channels and allows us to evaluate the effects of riblets (Endrikat *et al.* 2021*b*).

3. Effects of large riblets on the flow

The two data sets of flow above large riblets from experiments and simulations have different outer Reynolds numbers (tables 1, 2), but they complement each other at matched s^+ in the common physical and spectral regions analysed in this section. We first consider velocity spectra and then the mean flow.

3.1. *Riblets damp large-scale motions near the wall*

Figure 3 shows streamwise spectra of the streamwise velocity component at different heights for three riblet sizes (rows) and two spanwise positions (columns). The spectra demonstrate that large riblets reduce the energy of large-scale motions close to the wall relative to smooth-wall flow. A particularly clear example of this is given in figure 3(*e,f*), which shows the largest s^+ case. Here, if we compare the filled contours for the riblets with the grey line contours of the smooth wall, we see substantial missing large-scale energy near the wall at $\lambda_x^+ \approx 10\,000$–$50\,000$ and $(z - z_b)/k \lesssim 5$. Over a smooth-wall, long flow structures are coherent down to the viscous buffer region at $z^+ \approx 15$ (Hutchins & Marusic (2007), Monty, Harun & Marusic (2011), Squire *et al.* (2016*a*), and smooth-wall contours in figure 3). The large riblets, however, significantly weaken the near-wall part of long flow structures in figure 3. Even though these large motions lose energy as they scrape the riblets, the flow structures that scale with distance to the wall in the logarithmic region (Townsend 1976) appear intact (see dashed lines in figure 3, which show $\lambda_x = 30z$). The difference above the large riblets compared with smooth-wall flow is that flow structures scaling with wall distance seem to lack coherence with the wall.

The DNS spectra only extend to $\lambda_x^+ = L_x^+ \approx 2000$. The domain length is therefore too short to observe the energy difference at larger scales, but the spectra nevertheless show some of the energy reduction that riblets introduce. The DNS (red) contour lines in figure 3(*a–d*) run horizontally around $\lambda_x^+ \approx 1000$, where smooth-wall flow with vertical contour lines retains higher energy (only shown for smooth-wall experiments, but contour lines for smooth-wall DNS also run vertically).
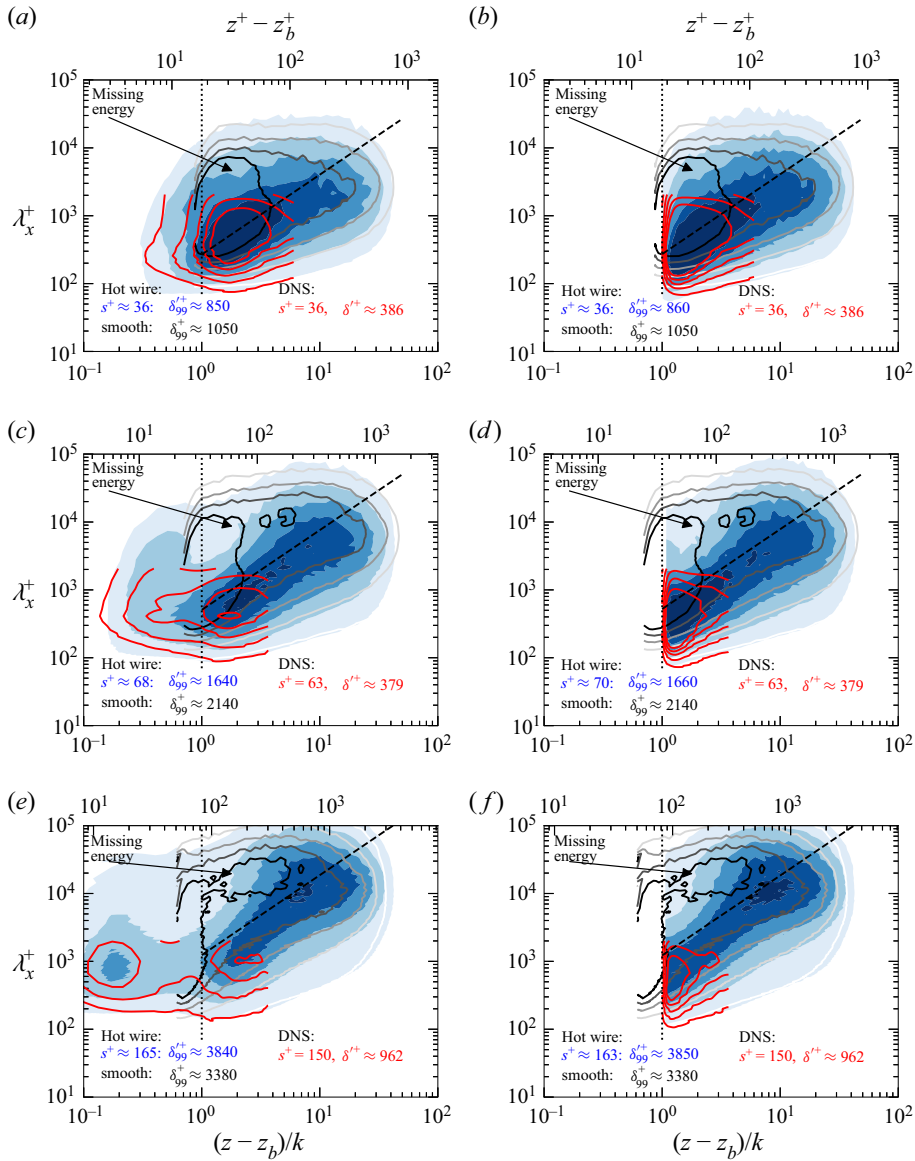
952 A27-8

Figure 3. Spectra of the turbulent component of streamwise velocity fluctuations (normalised by u_τ^2 and premultipied by the wavenumber k_x^+) with contour levels at $k_x^+ E_{uu}^{x+} = (0.2, 0.4, 0.6, 0.8, 1)$ for three riblet sizes at two spanwise positions: in the groove centre (a,c,e) and above the riblet tips (b,d,f). Contours (blue) are for hot-wire riblet data and red lines for DNS (drawn up to z_c). Bottom axes are normalised by the riblet height. Top axes show $z^+ - z_b^+$ for each hot-wire riblet case. For smooth-wall hot-wire contour lines (grey), z is normalised by k from the matching hot-wire riblet case and the origin is assumed at $(z - z_b)/k = 0.5$. Smooth-wall spectra in $(a–d)$ were recorded during the campaign by Wangsawijaya *et al.* (2020) in the same facility as the present riblet cases and smooth-wall spectra in (e,f) are from Chandran *et al.* (2017). Vertical dotted lines mark the riblet crest. Dashed lines represent $\lambda_x = 30z$ for $z_t < z < \delta_{99}'$. Arrows label a region of reduced energy around $\lambda_x \approx 5\delta_{99}'$.
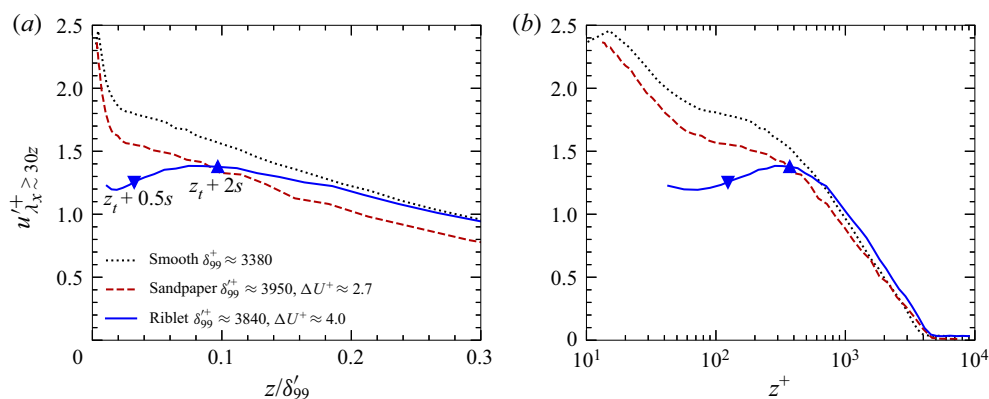
Figure 4. Energy of large-scale motions $\lambda_x \gtrsim 30z$ (integrated above the dashed line in figure 3e) that are damped by riblets relative to smooth-wall flow (Chandran *et al.* 2017) and sandpaper roughness (Squire *et al.* 2016b, case with $k_s^+ = 22$). Only showing the spanwise location above the riblet groove centre, starting at the height of the crest. Assuming a virtual origin with $\ell_t = k/2$.

Velocity fluctuations in and just above the riblet groove are well resolved in both hot-wire measurements and DNS (figure 3), which allows us to correct for the positional z error innate to hot-wire measurements by comparing to DNS data with well defined z/k. The z corrections, applied for all figures, are in the range $[-0.57, -0.4]$ mm in the groove centre and in the range $[-0.55, -0.12]$ mm at the riblet crest. As a reference, the riblet height $k = 1.365$ mm. All of these shifts are negative (i.e. downward), consistent with the tunnel floor being pulled upwards slightly by the flow and the probe support shifting downward slightly under aerodynamic loading. The corrections need not be exactly the same at both positions, because the probe is manually repositioned at each spanwise location using a z-positioning microscope (Titan Tool Supply), incurring different positioning errors.

In figure 4 we integrate spectra only over long wavelengths $\lambda_x \gtrsim 30z$, i.e. above the dashed line in figure 3. Comparison to smooth-wall flow with roughly matching $\delta_{99}'^+$ illustrates the reorganisation of near-wall turbulence. The large riblets significantly reduce the streamwise energy of large-scale motions at riblet-scaled heights of at least $z \lesssim z_t + 2s$ (or, equivalently, $z \lesssim z_b + 5k$ as in figure 3) and at outer-scaled heights $z \lesssim (0.1–0.2)\delta_{99}'$, i.e. into the logarithmic layer. The sandpaper roughness investigated by Squire *et al.* (2016b), shown by red dashed lines in figure 4, also reduces large-scale energy, but markedly less so than the riblets. The near-wall energy reduction of large flow structures by riblets in figures 3 and 4 is noticeable even at heights above the riblet-induced spanwise inhomogeneity of the mean flow, which we analyse in the following section.

3.2. *Roughness sublayer of the mean flow*

The mean flow $U^+(y, z)$, measured at two spanwise positions of the riblet groove, indicates the extent of the roughness sublayer in figure 5: the two profiles overlap for $z \gtrsim z_t + k$ (above the dotted line) in both experiments and DNS. An exception is the $s^+ = 36$ hot-wire profile at the tip position, which differs from the DNS data and does not fully join the hot-wire profile in the groove centre (figure 5a). The mismatch indicates experimental errors for the tip profile, because the DNS profiles for the same $s^+ = 36$ in figure 5(a) fit the trend observed for all other cases in both data sets: riblet-induced
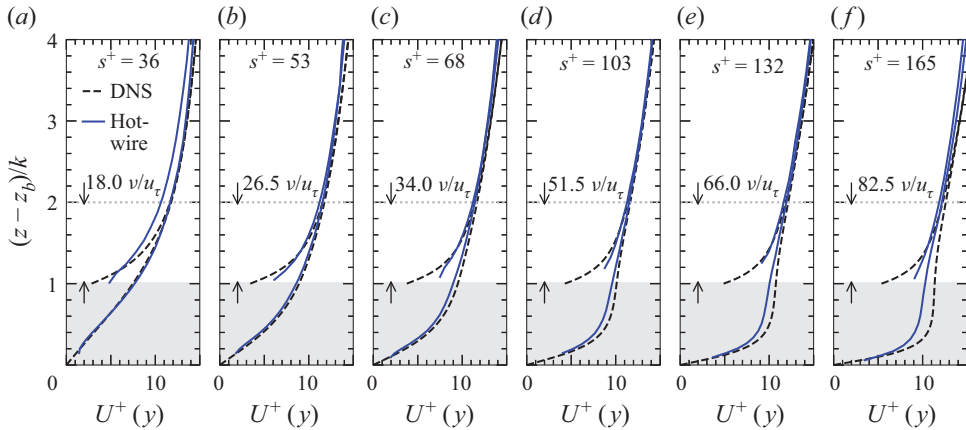
952 A27-10

Figure 5. Mean streamwise velocity at two spanwise positions: $y = 0$ (at the riblet tips) and $y = s/2$ (in the groove centre). Direct numerical simulation profiles are averaged in y only over the $0.18s$ covered respectively by the hot-wire probe and, for this figure only, interpolated to match the experimental s^+. The portion of profiles shown is below z_c and, therefore, unaffected by the minimal domain width. The dotted horizontal line marks the approximate extent of the roughness sublayer based on mean-flow inhomogeneity.

spanwise variations of the mean flow are limited to heights $z \lesssim z_t + k = z_t + 0.5s$. The scale separation between the height of the roughness sublayer of the mean flow and $\delta'_{99} \approx 47k$ (table 1) is therefore large in our experiments. Nevertheless, the effect of riblets on the turbulence structure (at least $z \lesssim z_t + 4k$, § 3.1) extends far beyond the spanwise variations of the mean flow.

Scaling of the mean-flow roughness sublayer with the horizontal roughness spacing as in figure 5 (with $0.5s = k$) has more generally been observed for canopy roughness (e.g. Raupach *et al.* 1980), streamwise ridges (e.g. Wang & Cheng 2006; Hwang & Lee 2018), sinusoidal roughness (Chan *et al.* 2018) and smaller riblets (Modesti *et al.* 2021). The blocking effect of a smooth wall causes large eddies to mostly produce wall-parallel (inactive) motions (Townsend 1976), but large riblets interact with lateral flow to create mean secondary motions in the cross-stream plane (Goldstein & Tuan 1998; Modesti *et al.* 2021). Therefore, a convenient measure of the roughness sublayer in DNS is the extent of dispersive (form-induced) stresses due to time-averaged secondary flows. These motions are not defined instantaneously, but they can be sensed statistically as dispersive Reynolds stresses that extend to heights of about half the horizontal roughness period (Chan *et al.* 2018; Modesti *et al.* 2021).

In figure 6(a) we confirm, for the present large riblets, that the dispersive Reynolds stresses of secondary flows (indicating mean-flow inhomogeneity) are limited to $z \lesssim z_t + (0.4\text{–}0.8)s$, depending on the threshold. Dispersive stresses of blunt, scalloped riblets are confined to similar heights (Rastegari & Akhavan 2018, figure 5(f) $s = 0.288\delta$). The peak value of dispersive stresses in figure 6(b) increases with s^+, but approaches a maximum (the negative of viscous-scaled Reynolds shear stress is less than 1). The same trend is evident in the time-averaged cross-flow of figure 7, which strengthens with increasing s^+, as discussed by Modesti *et al.* (2021). Furthermore, the roughness sublayer of the two-scale riblets (dashed lines in figure 6a) also scales with s, even though the additional half-height riblet in the groove visibly displaces turbulence upwards in figure 7(g–j) compared with the single-scale riblets in figure 7(a–d). The displacement of turbulence and the reduction of dispersive stresses by two-scale riblets in figure 6(b) reduce ΔU^+ at matched s^+ (following the drag decomposition from, e.g. Modesti *et al.*
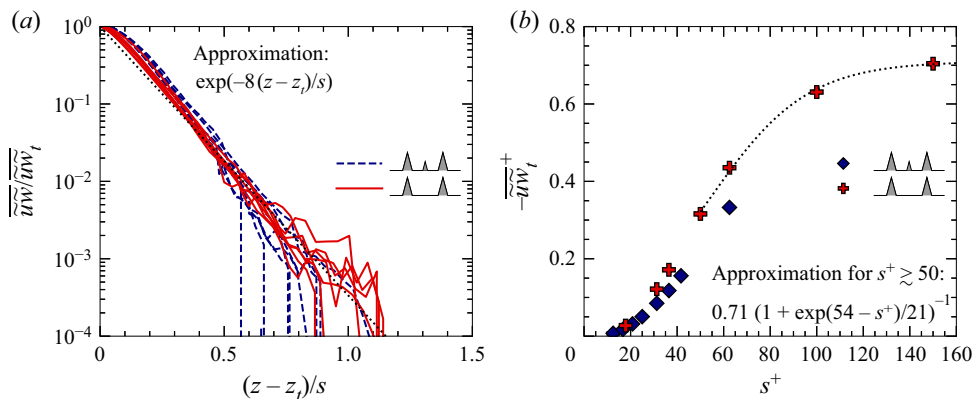
952 A27-11

Figure 6. The extent of DNS dispersive stresses defines the roughness sublayer of mean secondary flows. Profiles of dispersive stresses against z/s (a) collapse when shown relative to their respective peak value at the riblet tips $-\overline{\tilde{u}\tilde{w}}_t^+$ (b). This is similar to the coherent component of pressure fluctuations analysed by Seo, García-Mayoral & Mani (2015). Dotted lines are empirical approximations.
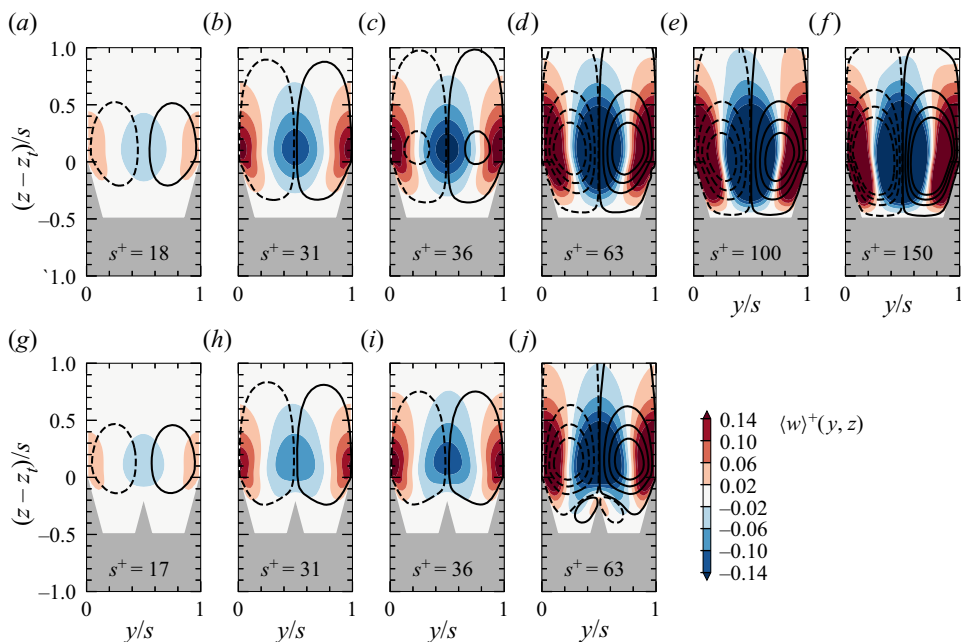

Figure 7. Cross-flow averaged in time, the streamwise direction and over riblet periods. Contours show wall-normal velocity and lines show the stream function $\psi^+ - \psi_w^+ = \pm(1, 21, 41, 61) \times 10^{-4}$ relative to $\psi_w^+ = 0$ on the wall (—— for counterclockwise rotation and - - - - for clockwise rotation).

(2021), and shown in §4). However, in §4 we consider different measures of the riblet size and demonstrate that the half-height riblets do not actually provide an overall drag benefit compared with the single-scale trapezoidal riblets once their size is scaled appropriately.

3.3. *Mean velocity in the logarithmic layer*

As shown in the previous section, spanwise variations of the mean flow in the roughness sublayer are confined to about $z \lesssim z_t + k$, but we next observe that the mean flow U^+ is
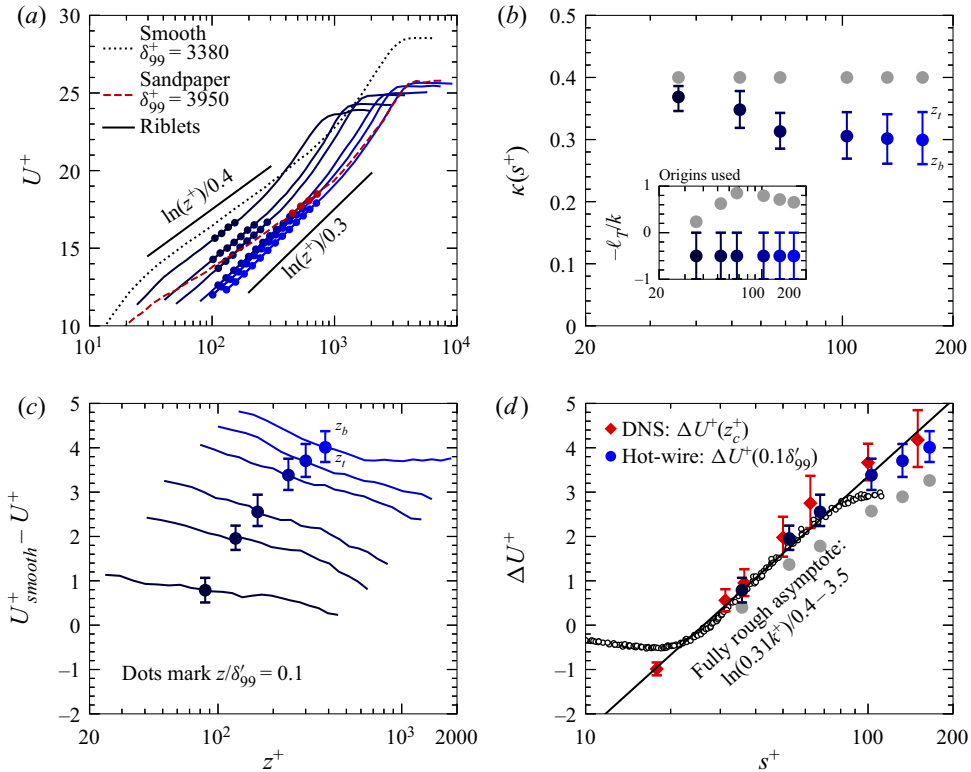
Figure 8. (*a*) Mean streamwise velocity from hot-wire measurements with a virtual origin $\ell_t = k/2$. Only showing the spanwise invariant flow above the roughness sublayer (figure 5). Filled circles mark measurements that are considered to lie within the logarithmic region (lower bound: $z^+ = \max(100, z_t^+ + 0.5s^+)$, upper bound: $z = 0.19\delta_{99}'$). Red dashed line: sandpaper roughness for which u_τ is measured with a drag balance (Squire *et al.* 2016*b*, $k_s^+ = 22$, $\delta_{99}^+ \approx 3950$, $\Delta U^+ \approx 2.7$, $\delta/k \approx 384$ and $\kappa \approx 0.378$). Dotted line: smooth-wall flow (Chandran *et al.* 2017). Error bars in (*b*–*d*) are for virtual origins between the groove bottom z_b ($\ell_t = k$) and the riblet crest z_t ($\ell_t = 0$). (*b*) Fitting parameter $\kappa(s^+)$ that describes the slope of the logarithmic region (dots in *a*) as a function of the riblet spacing. The fit only marginally depends on the choice of the lower bound. (*c*) Roughness functions using smooth-wall hot-wire data from Marusic *et al.* (2015), Chandran *et al.* (2017), Wangsawijaya *et al.* (2020) and Ramani *et al.* (2020) are only shown above the roughness sublayer and up to $z = \delta_{99}'/2$. (*d*) Drag curve as measured in (*c*). Direct numerical simulation values are measured at z_c and matched L_y to cancel out minimal-channel effects. Empty circles are for thicker trapezoidal riblets with $\alpha = 53.5°$ from Gatti *et al.* (2020, figure 4).

nevertheless modified in the spanwise homogeneous logarithmic layer, where the present riblets damp large-scale energy.

3.3.1. *Increased slope of the mean velocity profile*

Figure 8(*a*) shows a hot-wire velocity profile above a smooth wall (·····), for which the slope in the logarithmic region is well known to be described by the von Kármán constant $\kappa \approx 0.40$. The riblet-flow profiles in figure 8(*a*) are only shown in the spanwise uniform region above the roughness sublayer (figure 5) and we assume a virtual origin at the mid-point of the groove ($\ell_t = k/2$) for these profiles. The highlighted logarithmic region in figure 8(*a*) shows a clear trend of increasing slope with increasing riblet size for this choice of the virtual origin. The outer layers of the flow above the present large riblets and smooth wall are therefore not similar. Figure 8(*a*) additionally shows a velocity profile above sandpaper roughness from Squire *et al.* (2016*b*), with the same definition of the

virtual origin, as an example of rough-wall flows that commonly have the same $\kappa \approx 0.40$ as smooth-wall flows.

In figure 8(*b*) we measure the slope of the hot-wire mean profile by fitting a line to the logarithmic region. A reduction in κ with increasing s^+ is clearly visible for any virtual origin between the groove bottom and the riblet crest (error bars). Even with the origin at the riblet crest (top of the error bars), $\kappa \approx 0.34$ for the largest riblets. To illustrate the effect of the origin on the apparent local value of $\kappa = (z^+ \mathrm{d}U^+/\mathrm{d}z^+)^{-1}$, consider a fixed measurement location in the logarithmic layer. A higher origin reduces the distance z^+ between the measurement location and the virtual origin, increasing κ. In a similar manner, the positional adjustment applied to the hot-wire locations z in § 3.1, which accounts for the wall and probe-support movement under aerodynamic load, also slightly increased κ relative to the raw data. The friction velocity used for the riblet profiles is measured with a drag balance (§ 2.1) and could include an error. If we were to reduce u_τ to match the DNS profiles in figure 5, the apparent local value of κ would reduce further.

In hot-wire boundary-layer studies u_τ and the virtual origin are generally found by forcing $\kappa = 0.4$ (or a close value like $\kappa = 0.384 \pm 0.005$ as determined by Nagib & Chauhan 2008). However, with u_τ fixed by drag-balance measurements and z-positional errors corrected by comparing to spectra and mean profiles from DNS (§ 3.1), the position of the virtual origin is the only variable affecting κ. Forcing $\kappa = 0.4$ requires the origin to be about $0.7k$ above the riblet crest (see grey dots in the inset of figure 8*b*), which seems unrealistic. Other studies of roughness (e.g. Raupach *et al.* 1991; Grimmond & Oke 1999) and small s^+ riblets (e.g. Luchini *et al.* 1991; Endrikat *et al.* 2021*a*) use various definitions, but all place the virtual origin below the roughness crest, as summarised by Chung *et al.* (2021). Therefore, reasonable adjustments to the virtual origin or to u_τ cannot force $\kappa \approx 0.4$, which provides confidence that κ is indeed a function of s^+ for the present large riblets, as shown in figure 8(*b*).

3.3.2. *Outer-layer similarity*

Breugem, Boersma & Uittenbogaard (2006) and Suga *et al.* (2010) observe reduced κ above the permeable walls of porous surfaces at low friction Reynolds numbers ($\delta^+ \lesssim 678$ and $\delta^+ \lesssim 432$, respectively) and suggest the changes to the mean profile may be due to the wall-normal permeability of their surfaces. Small riblets can be interpreted as behaving similar to a porous surface, with an effective porosity that increases with riblet size (García-Mayoral & Jiménez 2011*b*; Endrikat *et al.* 2021*a*). Reasoning for reduced κ above permeable surfaces may therefore also be applicable to riblets. However, Manes *et al.* (2011) show that insufficient separation between inner and outer length scales explains the trend of reducing κ in the studies by Breugem *et al.* (2006) and Suga *et al.* (2010), in which the roughness sublayer based on Reynolds stresses induced by the wall porosity likely extends into the logarithmic layer.

For the present riblets, the roughness sublayer based on the extent of wall-parallel inhomogeneity of the mean flow is limited to $z \lesssim z_t + k$ (figure 5). This extent of the direct influence of riblets is small in outer units for all our experimental cases (table 1), suggesting that outer-layer similarity should exist above $z \approx z_t + k$ contrary to what we observe in figure 8. One way to rule out insufficient scale separation for the present riblets would be to repeat the experiments at matched s^+, but at an even higher δ/k (Chung *et al.* 2021), which is not possible with the current set-up. Nevertheless, unlike the surfaces that have been demonstrated to recover outer-layer similarity at larger scale separation (Krogstad & Efros 2012; Flack & Schultz 2014; Nugroho *et al.* 2021), the present riblets lack an obvious larger scale that could limit outer-layer similarity by farther extending the

roughness sublayer of the mean flow. In this sense, the present riblets are exceptional. In fact, the scale separation for the experimental data $\delta'_{99}/k \approx 47$ is roughly constant (table 1), but κ reduces nevertheless as δ'^{+}_{99} and k^{+} increase (figure 8b).

If the damped large-scale streamwise energy is interpreted as a roughness sublayer of turbulence, the affected region $z \lesssim z_t + 4k$ (figure 4) agrees with estimates of the roughness-sublayer height by, for example, Jiménez (2004) and Lee & Sung (2007). In § 3.4 we propose a connection between the damped large-scale energy and the changes to $\mathrm{d}U^{+}/\mathrm{d}z^{+}$ and κ that have been noted in figure 8 to persist beyond heights at which mean-flow homogeneity has recovered. However, since $\delta'_{99}/k \approx 47$ is roughly constant for all experimental riblet cases (table 1), we cannot discern if the wall-normal extent of large-scale energy reduction scales with the riblet size (e.g. these large scales are damped at heights $(z - z_b) \lesssim 5k$, as in figures 3, 4) or if it scales with the boundary-layer thickness (e.g. these large scales are damped near the wall at $z \lesssim (0.1\text{–}0.2)\delta'_{99}$, as in figure 4$a$). Consequently, it is not clear if increasing the scale separation δ'_{99}/k would restore outer-layer similarity in an increasingly large part of the logarithmic layer.

3.3.3. *Roughness function*
The mean velocity shifts $U^{+}_{smooth} - U^{+}$ for hot-wire profiles, shown in figure 8(c) and calculated with smooth-wall data for almost matching δ'^{+}_{99}, are visibly decreasing in the logarithmic region for the larger riblet cases. Although the range of uncertainty in ΔU^{+} measured at different heights is only about 1, the clearly increased logarithmic slope for the large riblets challenges our fundamental understanding and expectation of outer-layer similarity. Consequently, the velocity deficit relative to smooth-wall flow ΔU^{+} may not be an accurate measure of the drag change for these large riblets and, hence, cannot be easily extrapolated to full scale.

If we nevertheless measure a value for ΔU^{+} at an otherwise appropriate height of $z = 0.1\delta'_{99}$, the drag curve in figure 8(d) closely matches that from experimental channel flow data by Gatti *et al.* (2020) for $s^{+} \lesssim 80$ (inferred from the pressure drop, as profile measurements are not available). At larger $s^{+} \approx 100$, our riblets with tip angle $\alpha = 30°$ have higher drag than the data for $\alpha = 53.5°$ of Gatti *et al.* (2020). If we force $\kappa = 0.4$ by adjusting the virtual origin, the drag curve (grey dots in figure 8d) deviates significantly from the reference data at all s^{+}. The large deviation from the drag curve of similar riblets supports the assumption that a virtual origin far above the riblet crest is unphysical.

We further show a fully rough asymptote for reference in figure 8(d), even though riblets do not experience pressure drag, which is generally considered a prerequisite for fully rough behaviour. Riblets appear to approach fully rough behaviour (Jiménez 2004), but, as discussed by Gatti *et al.* (2020), only for a finite range of large s^{+} before the drag curve departs from the fully rough asymptote. The same trend can be discerned in the present data, although at higher s^{+} for the sharper geometry ($\alpha = 30°$ instead of $\alpha = 53.5°$). Furthermore in § 3.5 we see that the friction-scaled velocity at the crest, which would be constant in the fully rough regime, instead continues to increase with increasing s^{+}. Direct numerical simulation values of ΔU^{+} in figure 8(d) agree well with the experiments, within the expected uncertainties.

3.4. *Spectral shortcut linking damped large scales and altered mean profile*
The reduced large-scale energy (§ 3.1) extends into the logarithmic layer ($z \lesssim (0.1\text{–}0.2)\delta'_{99}$ and at least $z \lesssim z_t + 4k$), but riblet-induced spanwise velocity variations are limited to

$z \lesssim z_t + k$ (§ 3.2). In the following, we therefore hypothesise that the large-scale energy is transferred to secondary motions close to the wall, where large flow structures laterally scrape the riblets. We then propose that this reorganisation of turbulence could be associated with the unusually low $\kappa \approx 0.3$ (§ 3.3).

3.4.1. *Spectral shortcut mechanism*

The energy carried by dispersive Reynolds shear stresses increases with increasing s^+ (figure 6b), which correlates with both the energy reduction around $\lambda_x \approx 5\delta'_{99}$ (figures 3, 4) and the reduction of κ (figure 8b). However, the dispersive fluctuations of secondary flows cannot be measured by a single probe and, therefore, cannot be discerned from the spectra in figure 3. We nevertheless hypothesise that the reduction of large-scale streamwise energy by riblets compared with smooth-wall flow in experiments (discussed in § 3.1) is the result of a spectral shortcut as described by Finnigan (2000, figure 14) for wake production in plant canopies: Following Goldstein & Tuan (1998), the interaction of large flow structures ($\lambda_y \gtrsim s$) with riblets induces smaller flow structures of spanwise size $\lambda_y = s$, which appear as secondary motions in the time average and enhance cross-flow fluctuations in the roughness sublayer. Therefore, even without streamwise pressure drag that could damp the large-scale motions, riblets transfer energy directly from large-scale streamwise fluctuations to *s*-scaled Reynolds stresses of secondary flows. This accumulation of energy in the dispersive component at $\lambda_y = s$ is demonstrated, for example, by the cross-plane streamfunction contours in figure 7, that scale with the riblet spacing for all groove sizes. The interplay between turbulent and secondary motions is further supported by the study of Modesti *et al.* (2021), who decompose the drag change ΔU^+ and show that riblet surfaces with a large drag penalty due to secondary flows have a relatively low drag penalty due to purely turbulent velocity fluctuations and *vice versa*.

Zampiron, Cameron & Nikora (2021) describe a similar mechanism for the generation of secondary flows by triangular streamwise ridges. They decompose the stress balance equation for particle image velocimetry data and conclude that secondary flows extract energy from cross-flow velocity fluctuations, which in turn receive energy from turbulent streamwise fluctuations. Furthermore, the near-wall large-scale motions in the sandpaper study (isotropic roughness) of Squire *et al.* (2016b) are much less damped than over our riblets (figure 4), suggesting that anisotropic roughness elements (with some defined direction, like riblets) strengthen secondary motions. A clearer picture will have to await high-Reynolds-number measurements of secondary motions in the wall-parallel or cross-stream plane above riblets.

3.4.2. *Spectral shortcut at DNS-resolved scales*

The present hot-wire experiments resolve long enough flow structures to reveal a reduction of energy at scales $\lambda_x^+ \approx 10\,000$–$50\,000$ (figure 3e,f) that exceed typical numerical domains. However, some of the flow structures that interact with sufficiently large riblets to create secondary flows belong to the near-wall cycle ($\lambda_x^+ \approx 1000$ and $\lambda_y \gtrsim s$) and are resolved by both hot-wire measurements and DNS. Consequently, the energy reduction relative to smooth-wall flow observed in experiments (figure 4) is also evident at the largest scales resolved in the present DNS ($\lambda_x^+ \lesssim 2000$, table 2).

In figure 9 we subtract spectra from the DNS over a smooth wall from those over large riblets at matched heights above the virtual origin ($\ell_t = k/2$). Blue contours in figure 9(a,c) indicate a reduction of streamwise velocity fluctuations by riblets at super-riblet scales (i.e. larger-than-riblet scales) $\lambda_y \gtrsim 2s$, and red contours indicate an
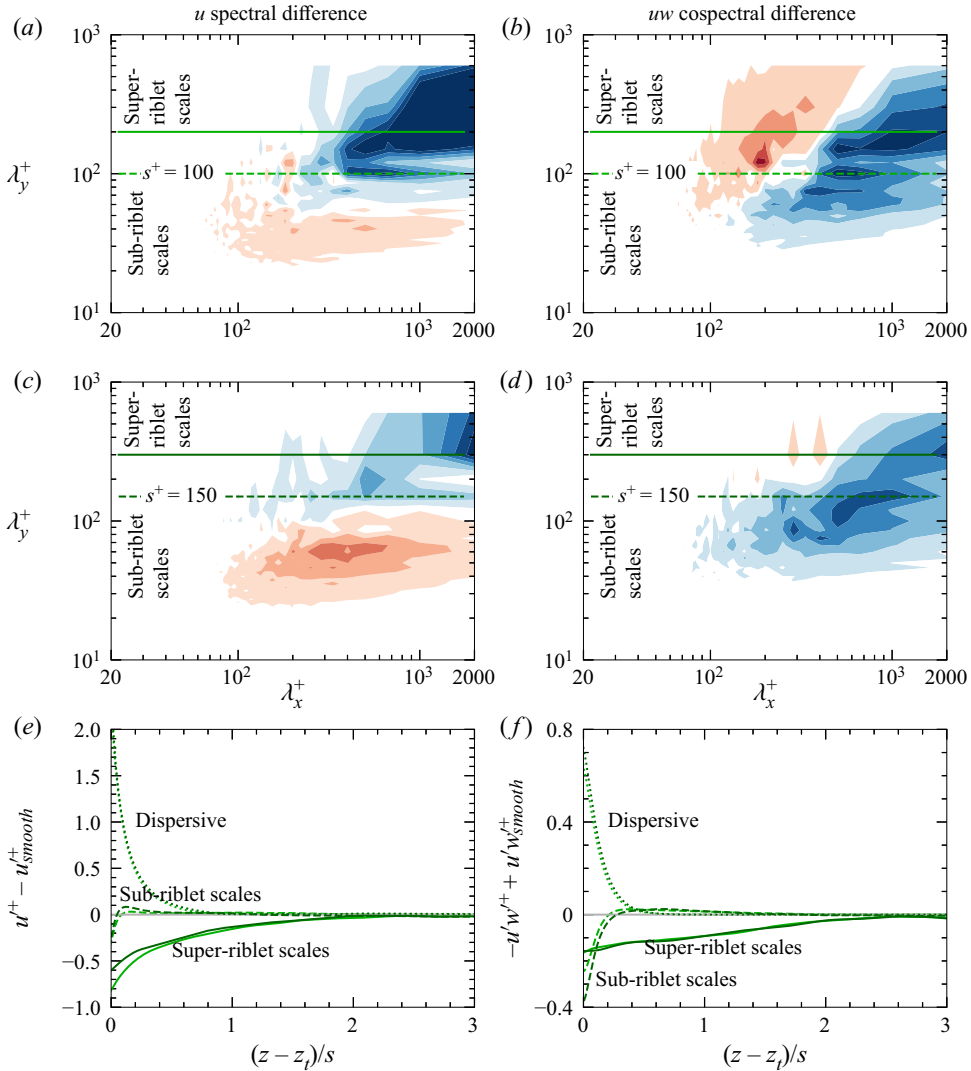
Figure 9. Premultiplied energy difference to smooth-wall flow $k_x^+ k_y^+ (E^+ - E_{smooth}^+)$ above large riblets with $s^+ = 100, 150$. Streamwise velocity fluctuations in (a,c,e) and Reynolds shear stress in (b,d,f). Two-dimensional spectra in (a–d) are at $z - z_t = 0.1s$. Contour levels range from blue (negative) to red (positive) between the limits $k_x^+ k_y^+ (E_{uu}^+ - E_{uu,smooth}^+) = \pm 0.22$ in steps of 0.04 (a,c) and $k_x^+ k_y^+ (-E_{uw}^+ + E_{uw,smooth}^+) = \pm 0.09$ in steps of 0.02 (b,d). The three integration regions for (e,f) are sub-riblet scales at $\lambda_y \lesssim s$ and $\lambda_x < \infty$, super-riblet (larger-than-riblet) scales at $\lambda_y \gtrsim 2s$ and the dispersive component at $\lambda_x = \infty$ and $\lambda_y = s$ including smaller scale harmonics. The threshold $2s$ is chosen for the super-riblet scales to only select the largest flow structures in the domain and avoid including energy at $\lambda_y \approx s$ that spills into adjacent modes.

increase of energy at sub-riblet scales $\lambda_y \lesssim s$. Figure 9(e) shows profiles of the integrated energy difference for the super-riblet scales, the sub-riblet scales and for the dispersive component. The solid lines for super-riblet scales in figure 9(e) are below zero, indicating large-scale energy reduction in DNS that is qualitatively the same as that seen in the hot-wire profiles (dotted smooth-wall profiles are above the solid riblet profiles in figure 4). In both data sets, energy of super-riblet scales is reduced at heights of at least $z - z_t \lesssim 2s$

or, equivalently, $z - z_b \lesssim 2.5s = 5k$. This extent is much greater than that of the dispersive fluctuations, which are also shown in figure 9(*e*).

3.4.3. *Spectral shortcut affects the mean velocity*

In DNS the energy reduction is likewise visible in Reynolds shear stresses (figure 9*b*,*d*,*f*). Large riblets reorganise some of the super-riblet-scale Reynolds shear stress to the dispersive component discussed in § 3.2 and shown again in figure 9(*f*), which only extends to heights $z \lesssim z_t + 0.5s$. Figure 9(*f*) therefore suggests that the spectral shortcut created by large riblets reorganises the turbulence by reducing super-riblet-scale Reynolds shear stresses at $z \lesssim z_t + 2s$ and increasing dispersive shear stresses closer to the wall at $z \lesssim z_t + 0.5s$. Although not measured in experiments, we can assume based on DNS that the largest s^+ riblets, shown in figure 4(*a*), reorganise Reynolds shear stress from super-riblet scales at $z/\delta'_{99} = 0.1$ in the logarithmic layer to dispersive stresses of s-scaled secondary flows below the logarithmic layer. The net reduction of Reynolds shear stress in the logarithmic layer is relatively small, but nevertheless accompanied by a clear increase of local dU^+/dz^+ or, correspondingly, a reduction of κ as observed in figure 8. Such a connection between damped large-scale energy and reduced κ is likewise demonstrated in numerical experiments by Jiménez (2022), in which the longest streaks in channel flow are artificially damped.

The even larger flow structures around $\lambda_x \approx 5\delta'_{99}$ in figure 3 are also damped by the spectral shortcut that acts on super-riblet scales, but they might not affect dU^+/dz^+, because such large flow structures do not contribute significantly to Reynolds shear stress at heights in the logarithmic layer $z \ll \lambda_x$ (Baidya *et al.* 2017; Kwon & Jiménez 2021) and are therefore ordinarily considered inactive at those heights (Townsend 1976).

3.5. *Scaling of the crest velocity*

Significant turbulence in the groove of riblets with $s^+ \gtrsim 60$ (figures 3, 7) suggests that a substantial part of the velocity deficit ΔU^+ is incurred below the riblet crest. In this section we therefore model the mean velocity at the riblet crest to crudely estimate the drag change $\Delta U^+(s^+)$ for a given riblet shape.

3.5.1. *Turbulence inside very large grooves*

The flow in the groove of small drag-reducing riblets is dominated by viscosity, but the wall at the bottom of very large grooves creates a secondary peak of sustained u fluctuations inside the groove, which we capture in spectra of both DNS and hot wire (figure 3*e*). The secondary peak at $\lambda_x^+ \approx 1000$ and $(z - z_b)/k \approx 0.18$ in the DNS, i.e. about 13 wall units above the groove bottom, suggests the formation of a nascent near-wall cycle inside the groove with $s^+ \gtrsim 100$, which is also partially visible for $s^+ = 63$ in figure 3(*c*). The emergence of a nascent near-wall cycle inside the groove of single-scale trapezoidal riblets with $s^+ \gtrsim 100$ agrees with the spanwise extent required to sustain near-wall turbulence in numerical experiments of narrow but doubly periodic smooth-wall channels (Jiménez & Moin 1991), even though the riblet grooves with no-slip side walls further constrain the flow. The half-height riblet in figure 7(*j*) displaces turbulence upwards in the groove compared with the single-scale riblets with the same spacing in figure 7(*d*) and presumably delays the formation of secondary near-wall turbulence to $s^+ \gtrsim 200$.
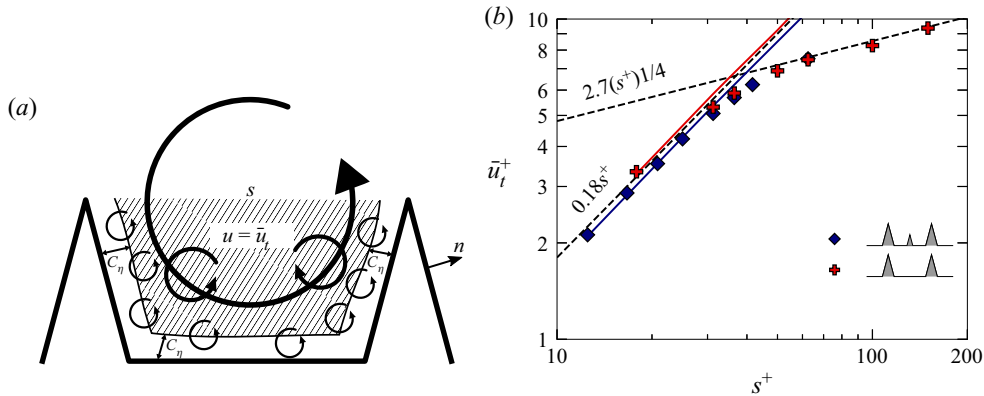
Figure 10. (*a*) Sketch of turbulent mixing in the groove of large riblets. (*b*) Streamwise velocity at the height of the riblet tips shown for the single-scale trapezoidal riblets, $A_w/A_p = 1.77$ and for the two-scale riblets $A_w/A_p = 2.15$ (the additional riblet increases the wetted area by a factor of 1.22). Solid lines show the laminar crest velocity for the two riblet shapes (as described by Modesti *et al.* 2021). Dashed lines are the power laws as labelled.

3.5.2. *Phenomenological model for the crest velocity*

In the following, we propose a phenomenological power law for the mean streamwise velocity at the height of the riblet tips $\bar{u}_t^+ \propto A_p/A_w(s^+)^{1/4}$, where the total wall plan area is A_p and the wetted area A_w. Figure 10(*b*) shows that the power law is consistent with values from our DNS for riblets with $s^+ \gtrsim 60$ and it therefore appears to capture the relevant flow physics in large riblet grooves.

Similar, but distinctly different scaling laws have been developed for roughness by Brutsaert (1975) and for superhydrophobic surfaces by Seo & Mani (2016), among others. Seo & Mani (2016) developed a 1/3-power law for the slip velocity of superhydrophobic surfaces with no-slip posts. They assume that a Prandtl–Blasius laminar-like boundary layer forms on each of the no-slip sections, which are spaced apart in the streamwise direction. This assumption is, of course, not valid for streamwise uniform riblets. The surface-renewal arguments of Brutsaert (1975) are developed for roughness, where temporarily stagnant eddies form in between the roughness elements. Here, diffusion limits the transport of a scalar from the stagnant eddies to the surface. Streamwise uniform riblets do not create such regions of stagnant flow, but viscous diffusion still limits the transport of momentum from the convecting eddies to the surface, an idea we use below.

For large riblet grooves, we envision an incipient turbulent Richardson–Kolmogorov cascade that mixes the momentum vigorously, except in the viscous sublayer enveloping the wetted wall. The well-mixed flow is assumed to have a velocity $\langle u \rangle = \bar{u}(z) + \tilde{u}(y, z) \approx \bar{u}_t$ that is uniform everywhere in the groove except in the wetted viscous boundary layer. In this unobstructed spectral region, the Kolmogorov cascade passes energy from size s to the dissipation length $\eta \equiv (\nu^3/\epsilon)^{1/4}$, where $\epsilon = K u_\tau^3/s$ is the dissipation rate of s-sized structures, with a constant K of $O(1)$. We assume $C\eta$ to scale the thickness of the viscous layer inside the groove with another constant C of $O(1)$ (sketched in figure 10*a*). With the velocity varying linearly inside the viscous layer, we can express the surface-perpendicular gradient by $\bar{u}_t/(C\eta)$. The drag is thus

$$\frac{D}{\rho} = A_w \nu \langle \frac{\partial u}{\partial n} \rangle_w \approx A_w \nu \frac{\bar{u}_t}{C\eta} = A_w \nu \frac{\bar{u}_t}{C} \left(\frac{\nu^3}{K u_\tau^3/s} \right)^{-1/4}, \tag{3.1}$$

952 A27-19

where $\langle \cdot \rangle_w = A_w^{-1} \int_w (\cdot) \, dS$ averages over the riblet wall and n is locally normal to the surface. The wall-shear stress $\tau_w/\rho = D/(\rho A_p) \equiv u_\tau^2$ and, therefore, to within an $O(1)$ constant,

$$u_\tau^2 \propto \frac{A_w}{A_p} \nu \bar{u}_t \left(\frac{u_\tau^3}{s\nu^3} \right)^{1/4} \Rightarrow \bar{u}_t^+ \propto \frac{A_p}{A_w} (s^+)^{1/4}. \tag{3.2}$$

Figure 10(*b*) shows that the crest velocity of the largest of our riblets indeed follows this trend, whereas the Stokes prediction for the crest velocity holds for smaller ($s^+ \lesssim 30$) riblets, $\bar{u}_t^+ = \ell_u^+ \propto s^+$, where ℓ_u is the streamwise protrusion height (Bechert & Bartenwerfer 1989; Luchini *et al.* 1991).

The crest velocity is only marginally affected by the secondary half-height riblet inside the groove at the present riblet sizes (figure 10*b*). For small sizes, the flow in the groove is dominated by viscosity and the secondary riblet has no noticeable effect on turbulence in the groove. In this regime, the 1/4-power law does not apply and the difference in A_w between the two surfaces does not significantly affect $\bar{u}_t$. At large riblet sizes with turbulence in the groove, the secondary riblet affects flow structures up to a height well above the riblet crest, where dispersive stresses in figure 6 are reduced compared with the single-scale riblets with the same spacing. The crest velocity, however, only captures the reorganisation of turbulent flow inside the groove. Therefore, even at $s^+ = 63$ of our largest two-scale riblets, the crest velocity does not yet reflect the geometry differences. At much greater riblet sizes, we would expect the half-sized additional riblets to reduce the crest velocity in proportion to the increased A_w in (3.2).

3.5.3. *Approximating ΔU^+*

For very small riblets ($s^+ \sim 0$), the roughness function is approximately constant from the crest upwards, as outlined by García-Mayoral *et al.* (2019) following the slip-lengths argument by Luchini (1996). Therefore, the crest (slip) velocity, along with the position of the virtual origin, describes the drag change ΔU^+ relative to a smooth wall (Ibrahim *et al.* 2021). For larger riblets, the drag change inferred at the crest is not an accurate measure, in part because the outer layers of the flow above the larger riblets studied here are not similar to smooth-wall flow. Furthermore, Gatti *et al.* 2020 do not observe fully rough behaviour, where the skin-friction coefficient would be independent of the Reynolds number. The present data also show a departure from the solid straight line in figure 8(*d*).

Nevertheless, we crudely estimate $\Delta U^+ \approx U_{t,Smooth}^+ - \bar{u}_t^+$ based on the velocity $\bar{u}_t^+ \approx a(A_p/A_w)(s^+)^{1/4}$ at the crest of large riblets ($s^+ \gtrsim 60$), with an empirical constant a. For the present trapezoidal riblets, $a(A_p/A_w) \approx 2.7$ (figure 10*b*). The corresponding smooth-wall velocity at the height of the riblet crest is $U_{t,Smooth}^+ \approx \ln(\ell_t^+)/0.4 + 5.1$ if $\ell_t \gtrsim 12$ as for our large riblets (table 2, assuming $\ell_t = k/2$). The approximation

$$\Delta U^+(s^+) \approx \ln(\ell_t^+)/0.4 + 5.1 - a(A_p/A_w)(s^+)^{1/4}, \quad \text{where } s^+ \gtrsim 60, \tag{3.3}$$

neglects variations in the roughness function above the crest and, therefore, overestimates ΔU^+ for our DNS cases by [1.63, 0.95, 0.54] at $s^+ = [63, 100, 150]$ and for the hot-wire cases by [1.87, 1.24, 0.98, 0.71] at $s^+ = [67, 102, 132, 165]$. Being valid for very large riblets, the approximation (3.3) approaches the value measured at z_c^+ (DNS) or $0.1\delta_{99}'$ (hot wire) as the riblet size increases.

952 A27-20

4. Drag-curve scaling for imperfectly repeated riblets

García-Mayoral & Jiménez (2011*b*) show that drag curves of single-scale riblets collapse reasonably well when the riblet size is expressed by the square root of the groove cross-sectional area ℓ_g^+. However, imperfectly manufactured riblets have a different drag curve and the riblet size of optimal drag reduction can generally not be estimated reliably based on the nominal riblet shape. The present two-scale trapezoidal riblets can be thought of as an idealised example of imperfectly repeated riblets, for which every other riblet is smaller than designed. If we compare the single-scale and two-scale riblets by matching s^+ (measured for the two-scale riblets between two of the perfectly repeated and in this case larger riblets), the additional half-height riblet reduces dispersive stresses and, therefore, drag (figure 6*b*). For a fair comparison, however, we have to use a suitable length scale for the two-scale (imperfectly manufactured) riblets.

The empirically derived riblet size ℓ_g^+ scales drag curves of single-scale riblets, because it is linearly proportional to the hydraulic (penetration) length ℓ_H^+ given by García-Mayoral & Jiménez (2011*b*) and García-Mayoral *et al.* (2019), which is a physics-based measure of the riblet size that accounts for the exact groove geometry. Curiously, ℓ_H^+ scales all drag curves despite being derived based on a Kelvin–Helmholtz-like instability that was later shown to only affect a subset of the riblet geometries (Endrikat *et al.* 2021*a*). The hydraulic length ℓ_H can be readily found for any two-dimensional riblet shape, including our two-scale riblets, by solving a Poisson equation in the cross-section of the riblet groove between the wall (subscript *w*) and the height of the riblet tips (subscript *t*),

$$\ell_H^3 = \frac{1}{s} \int_{A_g} f \, \mathrm{d}A, \quad \text{where} \quad \nabla_{yz}^2 f = -1 \quad \text{with} \quad \left. \frac{\mathrm{d}f}{\mathrm{d}z} \right|_t = 0, \quad \text{and} \quad f|_w = 0. \tag{4.1}$$

García-Mayoral & Jiménez (2011*b*) suggest that the wall-normal gradient of f should vanish at the height of the riblet tips (for not too shallow grooves) and that the no-slip boundary condition of velocity applies to f at the wall. We solve the same equation to find ℓ_H in the groove of our single-scale and two-scale riblets as well as the single-scale and two-scale ('brother-and-sister') blade riblets investigated by Bruse *et al.* (1993). For the two-scale surfaces, we consider the larger riblets to define the spacing s and groove size ℓ_g^+. The drag curves are shown in figure 11. Drag curves for different surfaces are closer together when we use ℓ_H^+ to characterise the riblet size (figure 11*b*) than with s^+ or ℓ_g^+ (figure 11*a,c*), based on the reduced size of the grey enveloping area. For the two-scale riblets, ℓ_H^+ is only poorly approximated by ℓ_g^+, suggesting that the square root of the groove area between the larger riblets, ℓ_g^+, does not characterise the drag regimes of two-scale riblets.

We propose a different geometric generalization of ℓ_H for two-scale riblets,

$$\ell_{g,i}^2 (k_1/k) = \begin{cases} A_g - (0.5A_g)(k_1/k) & \text{if } k_1 \lesssim k, \\ A_g - (0.5A_g)(k_1/k)^{-1} & \text{if } k_1 > k, \end{cases} \tag{4.2}$$

which depends on the ratio of the two riblet heights k_1/k. As for the single scale $\ell_g = \sqrt{A_g}$, we first need to calculate the groove cross-sectional area A_g, which is also a function only of k_1/k once the riblet size (e.g. s or k) is set. The fluid-filled groove area of the trapezoidal riblets is shaded in figure 12(*c–f*) and can be calculated by subtracting the area of the two
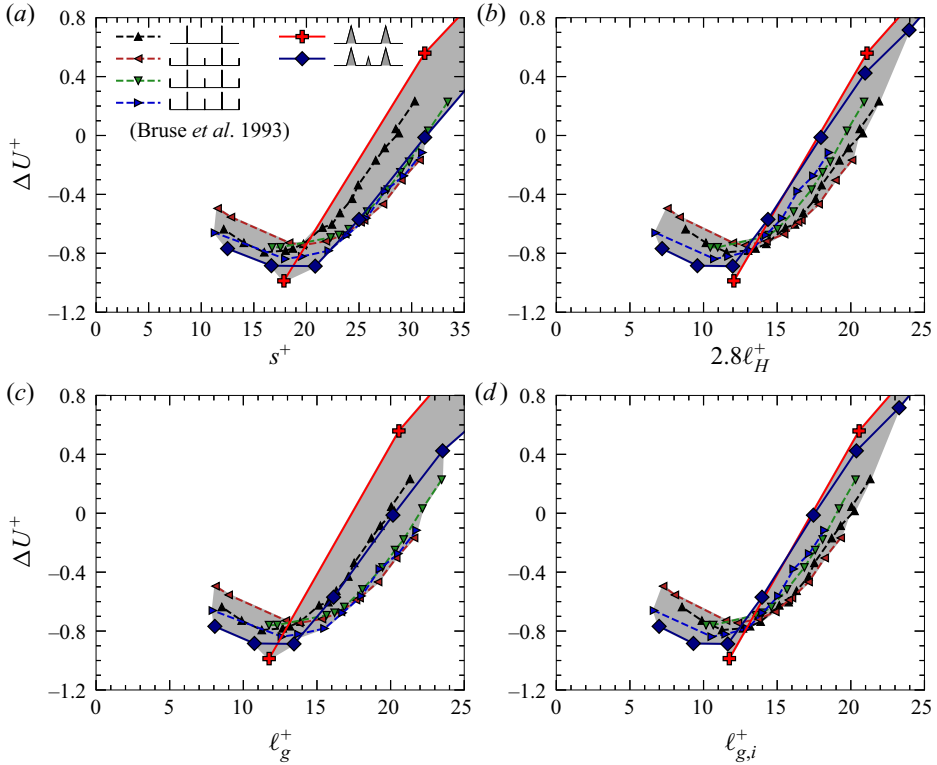
Figure 11. Drag curves for trapezoidal riblets (DNS, table 2) and blade riblets (from experiments by Bruse *et al.* 1993) with fixed $s/k = 2$. Experimental data are converted to ΔU^+ at a matched bulk-flow Reynolds number between the smooth and riblet wall and have heights $k_1/s = \{0, 0.2, 0.25, 0.3\}$. Each panel shows a different measure of the riblet size: (*a*) the (large) riblet spacing s^+, (*b*) the physics-based length ℓ_H^+ from (4.1) as suggested by García-Mayoral & Jiménez (2011*b*), (*c*) the square root of the whole groove cross-sectional area, (*d*) the geometrical length $\ell_{g,i}^+$ from (4.2).

solid-filled triangular regions from the entire rectangular area below the crest, i.e.

$$A_g = s \times \max(k, k_1) - k^2 \tan(\alpha/2) - k_1^2 \tan(\alpha/2) \quad \text{or} \tag{4.3}$$

$$A_g/k^2 = (s/k) \times \max(1, k_1/k) - \tan(\alpha/2) - (k_1/k)^2 \tan(\alpha/2), \tag{4.4}$$

if normalised by the main riblet height k. The ratio $s/k = 2$ and the tip angle $\alpha = 30°$ are fixed for the present riblets. The normalised groove area A_g/k^2 is therefore only a function of k_1/k. Similarly for the two-scale blade riblets from Bruse *et al.* (1993) with $s/k = 2$ and a thickness-to-spacing ratio $t/s = 0.01$,

$$A_g = s \times \max(k, k_1) - (t/s)sk - (t/s)sk_1 \quad \text{or} \tag{4.5}$$

$$A_g/k^2 = (s/k) \times \max(1, k_1/k) - (t/s)(s/k) - (t/s)(s/k)(k_1/k), \tag{4.6}$$

if normalised by the main riblet height k. To define the two-scale riblet size $\ell_{g,i}$ in (4.2), we linearly interpolate between the two extreme cases where the height of the smaller riblet is either $k_1 = 0$ or $k_1 = k$. Figure 12 shows both ℓ_g and $\ell_{g,i}$ as a function of k_1/k and the groove area A_g is shaded in figure 12(*c–f*). If $k_1 = 0$ as in figure 12(*c*), $\ell_{g,i}^2 = A_g$ is the same as ℓ_g^2. However, if the secondary riblets have the same height $k_1 = k$ as the main
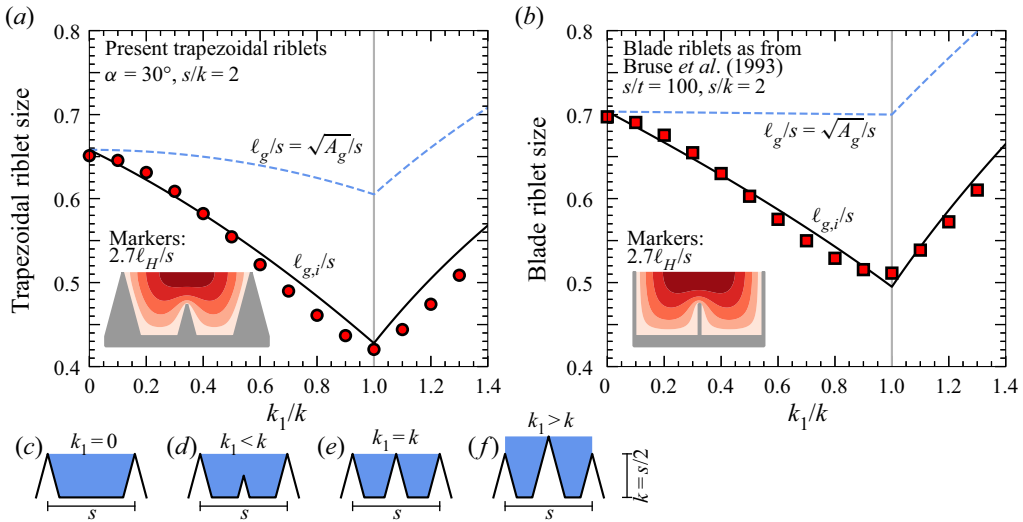
952 A27-22

Figure 12. Three definitions of the riblet size expressed relative to the spacing for trapezoidal riblets (a) and blade riblets (b). The main riblet has height $k = 0.5s$ and the additional riblet has the varying height k_1. The size of the whole groove A_g is shaded in the (c–f) and defines $\ell_g \equiv \sqrt{A_g}$ as suggested by García-Mayoral & Jiménez (2011b) for single-scale riblets. The interpolated size of two-scale riblets $\ell_{g,i}$ from (4.2) is closely proportional to the hydraulic length ℓ_H (markers) from (4.1). Insets in (a,b) show f of (4.1).

riblets, only half of the shaded area in figure 12(e) should be considered and $\ell_{g,i}^2 = 0.5A_g$. For heights $k_1 \lesssim k$ in between, we linearly interpolate the area $\ell_{g,i}^2 = A_g - (0.5A_g)(k_1/k)$ as in the first row of (4.2). We therefore consider less than the groove area A_g shaded in figure 12(d) to define the riblet size $\ell_{g,i}$. If $k_1 > k$ as in figure 12(f), the riblet spacing is related to the smaller riblet, because we maintain $s = 2k \neq 2k_1$. Therefore, $\ell_{g,i}/s$ from (4.2) is asymmetric with respect to $k_1/k = 1$ (figure 12a).

Using the newly defined $\ell_{g,i}^+$ to describe the groove size of two-scale riblets, drag curves in figure 11(d) collapse as they do when shown against ℓ_H^+ (figure 11b), i.e. the grey area enveloping the drag curves is almost identical. The curves for two-scale trapezoidal and blade riblets closely match their single-scale counterparts for post-drag-breakdown sizes and into the drag-increasing regime, i.e. for $\ell_{g,i}^+ \lesssim 20$. The ratio $\ell_{g,i}^+/\ell_H^+ \approx 2.7$ for the two-scale trapezoidal and blade riblets (markers in figure 12a,b), which is close to the ratio $\ell_g^+/\ell_H^+ \approx 2.8$ observed by García-Mayoral & Jiménez (2011b) for single-scale riblets. Describing the size of two-scale riblets by the empirical fit $\ell_{g,i}^+$ therefore seems to capture their drag characteristics, because it is closely proportional to the hydraulic scale ℓ_H^+. Conveniently, $\ell_{g,i}^+$ is a geometrical length found without having to solve the Poisson equation (4.1).

Seeing as ℓ_H scales the drag curves of single-scale riblets (García-Mayoral & Jiménez 2011b) and also of two-scale trapezoidal and blade riblets (figure 11b), we can assume that ℓ_H, or the proportional $\ell_{g,i}$, would likewise scale other imperfectly repeated riblets, because the Poisson equation (4.1) accounts for the exact geometry. For example, trapezoidal riblets with nominally equal height ($k_1 = k$) have $\ell_{g,i}/s = 0.428$ in figure 12(a), but a surface with some $k_1 < k$ and some $k_1 > k$ would have an average $\overline{\ell_{g,i}/s}$ that is larger. For the trapezoidal riblets, $\ell_{g,i}/s$ can be calculated for any ratio k_1/k by substituting (4.4) with $k = 0.5s$ into (4.2). As an example of manufacturing inaccuracies,

we consider a hypothetical surface with the two-scale trapezoidal riblets for which every other riblet k_1 is normal distributed with average $\overline{k_1} = k$ and most $k_1 \in [0.7, 1.3]k$ (two standard deviations equal $0.3k$), which is loosely based on the geometry measurements by Tiainen *et al.* (2020). With that distribution of k_1/k, the average $\overline{\ell_{g,i}/s} = 0.468$ is roughly 9 % greater than $\ell_{g,i}/s = 0.428$ for the perfectly manufactured surface with all $k_1 = k$. The imperfections therefore shift the surface to the right along the drag curve in figure 11(*d*). If the spacing s in physical units (μm) was chosen to reach the optimum at, for example, $\ell_{g,i}^+ = 11 < \overline{\ell_{g,i}^+}$ for given flow conditions, then the imperfect surface should be scaled down by $\ell_{g,i}/\overline{\ell_{g,i}}$ to achieve optimal drag reduction.

In general, calculating a few representative values of $\ell_{g,i}/s$ for an imperfectly manufactured riblet surface would approximate the average $\overline{\ell_{g,i}/s}$, which can then be used to account for surface imperfections by adjusting the riblet size. While this approach approximates the riblet size of optimal drag reduction, the actually achieved drag reduction at that size remains unknown and could only be found in laboratory experiments or DNS of imperfectly manufactured riblets with sufficiently many riblet periods across the span to attain statistical convergence.

5. Conclusions

We generated hot-wire and DNS data sets of flow over riblets of matched trapezoidal geometry for roughly the same range of spacings s^+ and observed close agreement of the near-wall flow. The riblet sizes are very large, such that most surfaces increase drag.

The present hot-wire measurements above large riblets show a reduction of large-scale energy around $\lambda_x \approx 5\delta_{99}'$ in the spectrum of purely turbulent streamwise velocity fluctuations (fluctuations about the local temporal mean) relative to smooth-wall flow at a matched Reynolds number (figures 3, 4). We hypothesise that the large-scale energy is reduced when long flow structures laterally scrape large riblets and transfer energy directly to smaller secondary flows of size $\lambda_y \approx s$, which have previously been identified in the time average (Goldstein & Tuan 1998; Modesti *et al.* 2021). A similar spectral shortcut was proposed by Finnigan (2000, figure 14) for wake production in plant canopies.

The reduction of large-scale energy extends into the logarithmic layer of the largest s^+ case ($z \lesssim (0.1\text{–}0.2)\delta_{99}'$ and at least $z \lesssim z_t + 4k$ in figure 4*a*), but spanwise variations of the mean velocity in hot-wire measurements (figure 5) and secondary mean flows in DNS (figures 6, 7) are limited to heights $z \lesssim z_t + k$. The present DNS further demonstrate that the large-scale energy reduction also applies to Reynolds shear stress (figure 9*f*). The hypothesised spectral shortcut therefore reorganises some Reynolds shear stresses from large flow structures in the logarithmic layer to secondary flows closer to the wall, below the logarithmic layer. This small net reduction of Reynolds shear stress in the logarithmic layer agrees with observations that the present large riblets modify the mean velocity even in the statistically spanwise uniform logarithmic layer. Specifically, we observe an increase of the logarithmic slope of the mean velocity profile in the logarithmic region, or equivalently, a decrease of the von Kármán constant κ from about 0.4 to about 0.3 for riblets with $s^+ \gtrsim 60$ (figure 8). The apparent value of κ is affected by the choice of virtual origin, but nevertheless in the range $0.26 \lesssim \kappa \lesssim 0.34$ for origins between the groove bottom and crest of the largest riblet case. Forcing $\kappa = 0.4$, as commonly done in hot-wire boundary-layer experiments, requires the virtual origin to be about $0.7k$ above the riblet crest, which would be unusual and probably unrealistic. The friction velocity, which generally also affects the apparent value of κ, is fixed by drag-balance measurements in the present experiments.

952 A27-24

The altered mean velocity profile questions the usefulness of ΔU^+ to characterise the drag change by trapezoidal riblets with $s^+ \gtrsim 60$. Nevertheless, the conservatively estimated uncertainty in ΔU^+ introduced by the z dependency of the roughness function in the logarithmic layer is only about 1 even for our largest case with $s^+ \approx 165$ (figure 8c). We also show that ΔU^+ as a function of $s^+ \gtrsim 60$ can be crudely estimated based on the velocity at the height of the riblet crest (figure 10) as $\Delta U^+ \approx \ln(\ell_t^+)/0.4 + 5.1 - a(A_p/A_w)(s^+)^{1/4}$, where we assume a virtual origin with $\ell_t = k/2$ and $a(A_p/A_w) \approx 2.7$ for the present trapezoidal riblets.

The addition of secondary half-height riblets in the groove prevents some turbulence from entering the groove and, thus, reduces drag at matched s^+. However, a new generalization of the hydraulic length ℓ_H (proposed by García-Mayoral & Jiménez (2011b) for single-scale riblets) collapses the drag curves of single-scale and two-scale trapezoidal riblets, demonstrating that the drag optimum is almost unaffected by the half-height riblet inside the groove. The two-scale riblets therefore illustrate that the drag curves of imperfectly repeated riblets can be scaled by ℓ_H (or by the roughly proportional $\ell_{g,i}$) to determine the optimal size for given flow conditions if representative measurements of the true geometry are available. In a hypothetical example of realistic manufacturing inaccuracies, riblets would need to be scaled down by 9 % to restore optimal drag reduction.

Declaration of interests. The authors report no conflict of interest.

Author ORCIDs.
- S. Endrikat https://orcid.org/0000-0002-8816-5445;
- R. Newton https://orcid.org/0000-0002-4923-3572;
- D. Modesti https://orcid.org/0000-0003-2214-5799;
- R. García-Mayoral https://orcid.org/0000-0001-5572-2607;
- D. Chung https://orcid.org/0000-0003-3732-364X.

Appendix. Effects of potential measurement errors

The active part of the hot wire is nominally 0.5 mm long and positioned in the middle between two riblets with spacing $s = 2.73$ mm (§ 2.1). The probe therefore averages the flow in the spanwise direction across a distance of $0.18s$. In this appendix we use the spatially resolved DNS data set to estimate the effects of probe misalignment within the riblet groove.

Figure 13(a,b) shows the effect of changing the length of the active part of the hot-wire probe on the mean streamwise velocity U^+ and its fluctuations u'^+, for a range of riblet sizes from the DNS data set. Doubling the probe length (width of the averaging area) only has minor effects on the measured profiles for both the mean and fluctuations. The most significant differences occur for the fluctuations above the largest riblets with $s^+ = 150$, particularly for the profile at the spanwise location above the riblet (blue, starting at the crest). Here, a wider probe measures lower fluctuation energy as u' is highest at the riblet crest and reduces along the spanwise direction towards the centre of the groove.
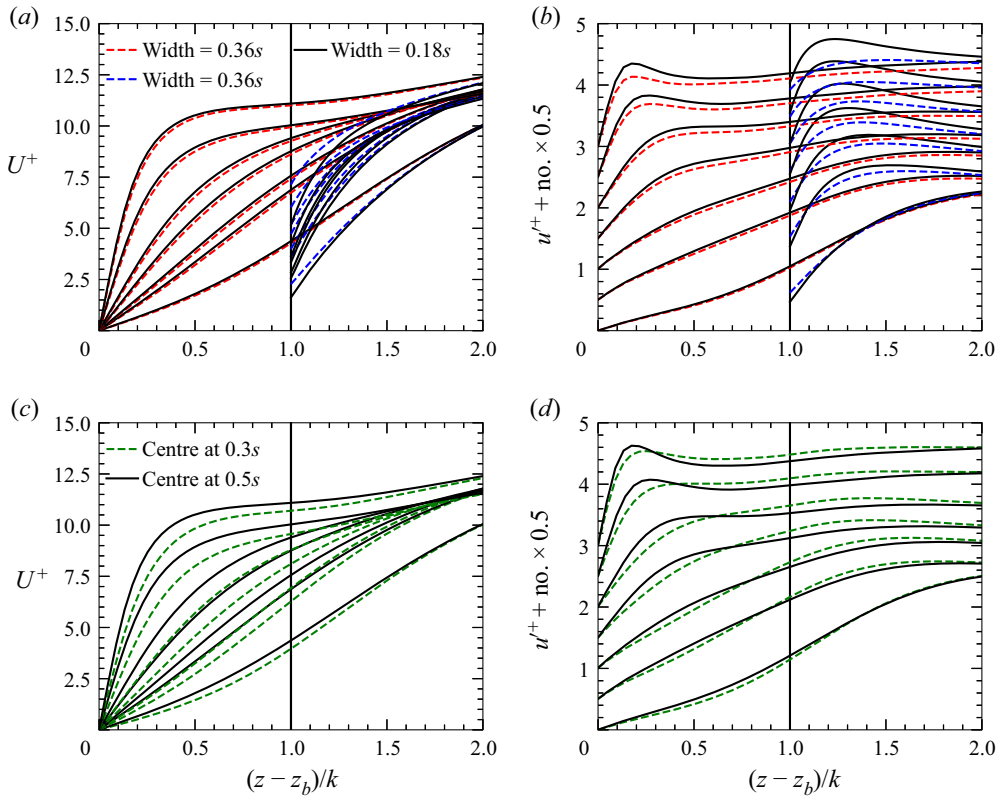
Figure 13. Estimating the effect of hot-wire probe errors based on DNS profiles of the mean streamwise velocity U^+ and the root-mean-square value $u'(z)$. (*a,b*) Influence of probe width for two spanwise positions evaluated in DNS data. The wide probe spans $0.36s$ (dashed) and the narrow probe spans $0.18s$ (solid). Red profiles starting at the bottom are taken in the centre of the groove (centre at $y = 0.5s$) and blue profiles starting at the crest are taken above the riblets (centre at $y = s$). (*c,d*) Influence of the spanwise probe location for a fixed probe width of $0.18s$. Fluctuations in (*b,d*) are shifted upwards by multiples of $0.5u_\tau$ to improve readability, but $u'(z = z_b) = 0$ as per the boundary condition.

A spanwise misalignment of the probe from its nominal position at $y = 0.5s$ is simulated in figure 13(*c,d*). Aligning the probe centre at an extreme $y = 0.3s$ (or $y = 0.7s$ conversely) reduces the mean velocity in the groove, because flow close to the no-slip groove side wall enters the average. Fluctuations are reduced in the lower half of the groove and increased around the riblet crest as the probe approaches the riblet laterally.

In summary, realistically expected spanwise misalignments of the probe and deviations from the nominal probe length are likely to have only negligible effects on the measured profiles of mean and fluctuating velocity. The alignment error in the wall-normal direction is more relevant for measurement comparisons.

REFERENCES

BAIDYA, R., PHILIP, J., HUTCHINS, N., MONTY, J.P. & MARUSIC, I. 2017 Distance-from-the-wall scaling of turbulent motions in wall-bounded flows. *Phys. Fluids* **29** (2), 020712.

BECHERT, D. & BARTENWERFER, M. 1989 The viscous flow on surfaces with longitudinal ribs. *J. Fluid Mech.* **206**, 105–129.

BECHERT, D., BRUSE, M., HAGE, W., VAN DER HOEVEN, J. & HOPPE, G. 1997 Experiments on drag-reducing surfaces and their optimization with an adjustable geometry. *J. Fluid Mech.* **338**, 59–87.

BREUGEM, W.P., BOERSMA, B.J. & UITTENBOGAARD, R.E. 2006 The influence of wall permeability on turbulent channel flow. *J. Fluid Mech.* **562**, 35–72.

BRUSE, M., BECHERT, D.W., VON DER HOEVEN, J.G.T., HAGE, W. & HOPPE, G. 1993 Experiments with conventional and with novel adjustable drag-reducing surfaces. In *Proc. Intl Conf. Near-Wall Turbul. Flow* (ed. R.M.C. So & C.G. Speziale), pp. 719–738.

BRUTSAERT, W. 1975 A theory for local evaporation (or heat transfer) from rough and smooth surfaces at ground level. *Water Resour. Res.* **11** (4), 543–550.

CHAN, L., MACDONALD, M., CHUNG, D., HUTCHINS, N. & OOI, A. 2018 Secondary motion in turbulent pipe flow with three-dimensional roughness. *J. Fluid Mech.* **854**, 5–33.

CHANDRAN, D., BAIDYA, R., MONTY, J.P. & MARUSIC, I. 2017 Two-dimensional energy spectra in high-Reynolds-number turbulent boundary layers. *J. Fluid Mech.* **826**, R1.

CHAVARIN, A. & LUHAR, M. 2019 Resolvent analysis for turbulent channel flow with riblets. *AIAA J.* **58** (2), 589–599.

CHOI, H., MOIN, P. & KIM, J. 1993 Direct numerical simulation of turbulent flow over riblets. *J. Fluid Mech.* **255**, 503–539.

CHU, D.C. & KARNIADAKIS, G.E. 1993 A direct numerical simulation of laminar and turbulent flow over riblet-mounted surfaces. *J. Fluid Mech.* **250**, 1–42.

CHUNG, D., CHAN, L., MACDONALD, M., HUTCHINS, N. & OOI, A. 2015 A fast direct numerical simulation method for characterising hydraulic roughness. *J. Fluid Mech.* **773**, 418–431.

CHUNG, D., HUTCHINS, N., SCHULTZ, M.P. & FLACK, K.A. 2021 Predicting the drag of rough surfaces. *Annu. Rev. Fluid Mech.* **53**, 439–471.

CLAUSER, F.H. 1956 The turbulent boundary layer. *Adv. Appl. Mech.* **4**, 1–51.

ENDRIKAT, S., MODESTI, D., GARCÍA-MAYORAL, R., HUTCHINS, N. & CHUNG, D. 2021*a* Influence of riblet shapes on the occurrence of Kelvin–Helmholtz rollers. *J. Fluid Mech.* **913**, A37.

ENDRIKAT, S., MODESTI, D., MACDONALD, M., GARCÍA-MAYORAL, R., HUTCHINS, N. & CHUNG, D. 2021*b* Direct numerical simulations of turbulent flow over various riblet shapes in minimal-span channels. *Flow Turbul. Combust.* **107**, 1–29.

FINNIGAN, J. 2000 Turbulence in plant canopies. *Annu. Rev. Fluid Mech.* **32** (1), 519–571.

FLACK, K.A. & SCHULTZ, M.P. 2014 Roughness effects on wall-bounded turbulent flows. *Phys. Fluids* **26** (10), 101305.

FLORES, O. & JIMÉNEZ, J. 2010 Hierarchy of minimal flow units in the logarithmic layer. *Phys. Fluids* **22** (7), 071704.

GARCÍA-MAYORAL, R., GÓMEZ-DE-SEGURA, G. & FAIRHALL, C.T. 2019 The control of near-wall turbulence through surface texturing. *Fluid Dyn. Res.* **51** (1), 011410.

GARCÍA-MAYORAL, R. & JIMÉNEZ, J. 2011*a* Drag reduction by riblets. *Phil. Trans. R. Soc. Lond.* A **369** (1940), 1412–1427.

GARCÍA-MAYORAL, R. & JIMÉNEZ, J. 2011*b* Hydrodynamic stability and breakdown of the viscous regime over riblets. *J. Fluid Mech.* **678**, 317–347.

GATTI, D., VON DEYN, L., FOROOGHI, P. & FROHNAPFEL, B. 2020 Do riblets exhibit fully rough behaviour? *Exp. Fluids* **61**, 81.

GOLDSTEIN, D. & TUAN, T.C. 1998 Secondary flow induced by riblets. *J. Fluid Mech.* **363**, 115–151.

GRIMMOND, C.S.B. & OKE, T.R. 1999 Aerodynamic properties of urban areas derived from analysis of surface form. *J. Appl. Meteorol.* **38** (9), 1262–1292.

HAM, F., MATTSSON, K. & IACCARINO, G. 2006 Accurate and stable finite volume operators for unstructured flow solvers. In *Center for Turbulence Research, Stanford University/NASA AMES, Annual Research Briefs* (ed. P. Moin & N.N. Mansour), pp. 243–261. Stanford University

HAM, F., MATTSSON, K., IACCARINO, G. & MOIN, P. 2007 Towards time-stable and accurate LES on unstructured grids. In *Complex Effects in Large Eddy Simulations* (ed. S.C. Kassinos, C.A. Langer, G. Iaccarino & P. Moin), pp. 235–249. Springer.

HAMA, F.R. 1954 Boundary-layer characteristics for smooth and rough surfaces. *Soc. Nav. Archit. Mar. Engrs* **62**, 333–358.

HARUN, Z., MONTY, J.P., MATHIS, R. & MARUSIC, I. 2013 Pressure gradient effects on the large-scale structure of turbulent boundary layers. *J. Fluid Mech.* **715**, 477–498.

HUTCHINS, N. & MARUSIC, I. 2007 Large-scale influences in near-wall turbulence. *Phil. Trans. R. Soc. Lond.* A **365** (1852), 647–664.

HUTCHINS, N., NICKELS, T.B., MARUSIC, I. & CHONG, M.S. 2009 Hot-wire spatial resolution issues in wall-bounded turbulence. *J. Fluid Mech.* **635**, 103–136.

HWANG, H.G. & LEE, J.H. 2018 Secondary flows in turbulent boundary layers over longitudinal surface roughness. *Phys. Rev. Fluids* **3**, 014608.

Hwang, Y. 2013 Near-wall turbulent fluctuations in the absence of wide outer motions. *J. Fluid Mech.* **723**, 264–288.

Ibrahim, J.I., Gómez-de-Segura, G., Chung, D. & García-Mayoral, R. 2021 The smooth-wall-like behaviour of turbulence over drag-altering surfaces: a unifying virtual-origin framework. *J. Fluid Mech.* **915**, A56.

Jiménez, J. 2004 Turbulent flows over rough walls. *Annu. Rev. Fluid Mech.* **36**, 173–196.

Jiménez, J. 2022 The streaks of wall-bounded turbulence need not be long. *J. Fluid Mech.*, **945**, R3.

Jiménez, J. & Moin, P. 1991 The minimal flow unit in near-wall turbulence. *J. Fluid Mech.* **225**, 213–240.

Kaakkunen, J., Tiainen, J., Jaatinen-Värri, A., Grönman, A. & Lohtander, M. 2018 Fabrication of surfaces with reduced friction using nanosecond laser. *Procedia Manuf.* **17**, 14–21.

Krogstad, P.-Å. & Efros, V. 2010 Rough wall skin friction measurements using a high resolution surface balance. *Intl J. Heat Fluid Flow* **31** (3), 429–433.

Krogstad, P.-Å. & Efros, V. 2012 About turbulence statistics in the outer part of a boundary layer developing over two-dimensional surface roughness. *Phys. Fluids* **24** (7), 075112.

Krogstadt, P.-Å. & Antonia, R.A. 1999 Surface roughness effects in turbulent boundary layers. *Exp. Fluids* **27** (5), 450–460.

Kwon, Y. & Jiménez, J. 2021 An isolated logarithmic layer. *J. Fluid Mech.* **916**, A35.

Lee, S.-H. & Sung, H.J. 2007 Direct numerical simulation of the turbulent boundary layer over a rod-roughened wall. *J. Fluid Mech.* **584**, 125–146.

Lee, S.J. & Lee, S.H. 2001 Flow field analysis of a turbulent boundary layer over a riblet surface. *Exp. Fluids* **30** (2), 153–166.

Ligrani, P.M. & Bradshaw, P. 1987 Spatial resolution and measurement of turbulence in the viscous sublayer using subminiature hot-wires probes. *Exp. Fluids* **5**, 407–417.

Luchini, P. 1996 Reducing the turbulent skin friction. *Comput. Meth. Appl. Sci.* **3**, 466–470.

Luchini, P., Manzo, F. & Pozzi, A. 1991 Resistance of a grooved surface to parallel flow and cross-flow. *J. Fluid Mech.* **228**, 87–109.

MacDonald, M., Chung, D., Hutchins, N., Chan, L., Ooi, A. & García-Mayoral, R. 2017 The minimal-span channel for rough-wall turbulent flows. *J. Fluid Mech.* **816**, 5–42.

MacDonald, M., Ooi, A., García-Mayoral, R., Hutchins, N. & Chung, D. 2018 Direct numerical simulation of high aspect ratio spanwise–aligned bars. *J. Fluid Mech.* **843**, 125–155.

Manes, C., Poggi, D. & Ridolfi, L. 2011 Turbulent boundary layers over permeable walls: scaling and near-wall structure. *J. Fluid Mech.* **687**, 141–170.

Marusic, I., Chauhan, K.A., Kulandaivelu, V. & Hutchins, N. 2015 Evolution of zero-pressure-gradient boundary layers from different tripping conditions. *J. Fluid Mech.* **783**, 379–411.

Modesti, D., Endrikat, S., Hutchins, N. & Chung, D. 2021 Dispersive stresses in turbulent flow over riblets. *J. Fluid Mech.* **917**, A55.

Monty, J.P., Harun, Z. & Marusic, I. 2011 A parametric study of adverse pressure gradient turbulent boundary layers. *Intl J. Heat Fluid Flow* **32** (3), 575–585.

Nagib, H. & Chauhan, K. 2008 Variations of von Kármán coefficient in canonical flows. *Phys. Fluids* **20**, 101518.

Napoli, E., Armenio, V. & De Marchis, M. 2008 The effect of the slope of irregularly distributed roughness elements on turbulent wall-bounded flows. *J. Fluid Mech.* **613**, 385–394.

Newton, R., Chung, D. & Hutchins, N. 2018 An experimental investigation into the breakdown of riblet drag reduction at post-optimal conditions. In *21st Australasian Fluid Mechanics Conference*.

Nugroho, B., Monty, J.P., Utama, I.K.A.P., Ganapathisubramani, B. & Hutchins, N. 2021 Non-*k*-type behaviour of roughness when in-plane wavelength approaches the boundary layer thickness. *J. Fluid Mech.* **911**, A1.

Pokrajac, D., Finnigan, J., Manes, C., McEwan, I. & Nikora, V. 2006 On the definition of the shear velocity in rough bed open channel flows. *River Flow* **1**, 89–98.

Ramani, A., Nugroho, B., Busse, A., Monty, J.P., Hutchins, N. & Jelly, T.O. 2020 The effects of anisotropic surface roughness on turbulent boundary-layer flow. In *22nd Australasian Fluid Mechanics Conference*, 7-10 Dec 2020, Brisbane, Australia.

Ran, W., Zare, A. & Jovanović, M.R. 2021 Model-based design of riblets for turbulent drag reduction. *J. Fluid Mech.* **906**, A7.

Rastegari, A. & Akhavan, R. 2018 The common mechanism of turbulent skin–friction drag reduction with superhydrophobic longitudinal microgrooves and riblets. *J. Fluid Mech.* **838**, 68–104.

Raupach, M.R., Antonia, R.A. & Rajagopalan, S. 1991 Rough-wall turbulent boundary layers. *Appl. Mech. Rev.* **44** (1), 1–25.

RAUPACH, M.R., THOM, A.S. & EDWARDS, I. 1980 A wind-tunnel study of turbulent flow close to regularly arrayed rough surfaces. *Boundary-Layer Meteorol.* **18** (4), 373–397.

SCHULTZ, M.P. & FLACK, K.A. 2009 Turbulent boundary layers on a systematically varied rough wall. *Phys. Fluids* **21** (1), 015104.

SEO, J., GARCÍA-MAYORAL, R. & MANI, A. 2015 Pressure fluctuations and interfacial robustness in turbulent flows over superhydrophobic surfaces. *J. Fluid Mech.* **783**, 448–473.

SEO, J. & MANI, A. 2016 On the scaling of the slip velocity in turbulent flows over superhydrophobic surfaces. *Phys. Fluids* **28** (2), 025110.

SHARMA, A. & GARCÍA-MAYORAL, R. 2020 Turbulent flows over dense filament canopies. *J. Fluid Mech.* **888**, A2.

SPALART, P.R. & MCLEAN, D. 2011 Drag reduction: enticing turbulence, and then an industry. *Phil. Trans. R. Soc. Lond.* A **369**, 1556–1569.

SQUIRE, D.T., MORRILL-WINTER, C., HUTCHINS, N., MARUSIC, I., SCHULTZ, M.P. & KLEWICKI, J.C. 2016*a* Smooth- and rough-wall boundary layer structure from high spatial range particle image velocimetry. *Phys. Rev. Fluids* **1**, 064402.

SQUIRE, D.T., MORRILL-WINTER, C., HUTCHINS, N., SCHULTZ, M.P., KLEWICKI, J.C. & MARUSIC, I. 2016*b* Comparison of turbulent boundary layers over smooth and rough surfaces up to high Reynolds numbers. *J. Fluid Mech.* **795**, 210–240.

SUGA, K., MATSUMURA, Y., ASHITAKA, Y., TOMINAGA, S. & KANEDA, M. 2010 Effects of wall permeability on turbulence. *Intl J. Heat Fluid Flow* **31** (6), 974–984.

SUZUKI, Y. & KASAGI, N. 1994 Turbulent drag reduction mechanism above a riblet surface. *AIAA J.* **32** (9), 1781–1790.

TIAINEN, J., GRÖNMAN, A., JAATINEN-VÄRRI, A. & PYY, L. 2020 Effect of non-ideally manufactured riblets on airfoil and wind turbine performance. *Renew. Energy* **155**, 79–89.

TOWNSEND, A.A. 1956 *The Structure of Turbulent Shear Flow*, 1st edn. Cambridge University Press.

TOWNSEND, A.A. 1976 *The Structure of Turbulent Shear Flow*, 2nd edn. Cambridge University Press.

TULLIS, S. & POLLARD, A. 1993 Modelling the time dependent flow over riblets in the viscous wall region. *Appl. Sci. Res.* **50**, 299–314.

VINUESA, R., PRUS, C., SCHLATTER, P., & NAGIB, H.M. 2016 Convergence of numerical simulations of turbulent wall-bounded flows and mean cross-flow structure of rectangular ducts. *Meccanica* **51** (12), 3025–3042.

WALSH, M. & WEINSTEIN, L. 1978 Drag and heat transfer on surfaces with small longitudinal fins. In *11th Fluid and Plasma Dynamics Conference*. AIAA Paper 1978–1161.

WANG, Z. & CHENG, N. 2006 Time-mean structure of secondary flows in open channel with longitudinal bedforms. *Adv. Water Resour.* **29** (11), 1634–1649.

WANGSAWIJAYA, D.D., BAIDYA, R., CHUNG, D., MARUSIC, I. & HUTCHINS, N. 2020 The effect of spanwise wavelength of surface heterogeneity on turbulent secondary flows. *J. Fluid Mech.* **894**, A7.

WEST, N., SAMMUT, K. & TANG, Y. 2018 Material selection and manufacturing of riblets for drag reduction: an updated review. *Proc. Inst. Mech. Engrs* **232** (7), 610–622.

ZAMPIRON, A., CAMERON, S. & NIKORA, V. 2021 Momentum and energy transfer in open-channel flow over streamwise ridges. *J. Fluid Mech.* **915**, A42.